

University of Central Florida

STARS

Electronic Theses and Dissertations, 2020-

2022

Characterizing the Effects of Porosity and Particle Size on TIR Emissivity Spectral Features of Olivine

Ryan Galinkin

University of Central Florida



Part of the [Astrophysics and Astronomy Commons](#)

Find similar works at: <https://stars.library.ucf.edu/etd2020>

University of Central Florida Libraries <http://library.ucf.edu>

This Masters Thesis (Open Access) is brought to you for free and open access by STARS. It has been accepted for inclusion in Electronic Theses and Dissertations, 2020- by an authorized administrator of STARS. For more information, please contact STARS@ucf.edu.

STARS Citation

Galinkin, Ryan, "Characterizing the Effects of Porosity and Particle Size on TIR Emissivity Spectral Features of Olivine" (2022). *Electronic Theses and Dissertations, 2020-*. 1201.
<https://stars.library.ucf.edu/etd2020/1201>

CHARACTERIZING THE EFFECTS OF POROSITY AND PARTICLE SIZE ON TIR
EMISSIVITY SPECTRAL FEATURES OF OLIVINE

by

RYAN GALINKIN

B.S. Rutgers, the State University of New Jersey, 2016

M.S. Rutgers, the State University of New Jersey, 2019

A thesis submitted in partial fulfillment of the requirements
for the degree of Master of Science
in the Department of Physics
in the College of Sciences
at the University of Central Florida
Orlando, Florida

Summer Term
2022

ABSTRACT

We generated a series of 15 particulate San Carlos olivine samples with varying porosity and particle size. We created five different particle size distributions and each particle size distribution was prepared with three different packing techniques. These samples were then imaged under a microscope and a binarization thresholding technique was used to determine each sample's surface porosity by the ratio of dark, void pixels to the total number of pixels in each image. Our results show that we could estimate surface porosity from the analysis of a microscopic image, a non-destructive technique. These samples were then placed in the Planetary Analogue Surface Chamber for Asteroid and Lunar Environments (PASCALE) and their thermal infrared (TIR) emissivity spectra were measured under ambient or Earth-like conditions. We selected key diagnostic spectral features and compared how these features changed with increased porosity and reduced particle size. From this investigation, we concluded that the spectral effects due to surface porosity and particle size could only be uniquely distinguished from one another when we observed shifts in the transparency feature due solely to changes in porosity.

TABLE OF CONTENTS

LIST OF FIGURES	vi
LIST OF TABLES	vii
1. INTRODUCTION	1
2. BACKGROUND	6
3. METHODS AND ANALYSIS	9
3.1 Sample Production and Particle Size Analysis	9
3.2 Sample Packing Methods	13
3.3 Sample Characterization	14
3.3.1 Bulk Porosity Calculation	14
3.3.2 Surface Porosity Calculation via Microscopic Imaging and Image Analysis	15
3.4 TIR Spectroscopy	17
4. RESULTS	26
4.1 Surface Porosity Estimations	26
4.2 Observed TIR Spectral Changes due to Surface Porosity	27
4.3 Observed TIR Spectral Changes due to Particle Size	30
4.4 Differences Between Surface Porosity and Particle Size	34
5. DISCUSSION	36
5.1 Porosity Estimations and Uncertainties	36
5.2 Unexpected Behavior due to Surface Porosity Spectral Effects	37
5.3 Future Investigations	38
6. CONCLUSIONS	41

APPENDIX A: CUMULATIVE PARTICLE SIZE WEIGHTS	42
APPENDIX B: DEPOSITED SAMPLE SIEVE SIZE DISCUSSION	44
APPENDIX C: HIGH WAVENUMBER TRANSPARENCY SLOPE VS. DEPTH OF THE 3 RD VIBRATION BAND	47
APPENDIX D: HIGH WAVENUMBER TRANSPARENCY SLOPE VS. CF SPECTRAL DEPTH.....	49
APPENDIX E: HIGH WAVENUMBER TRANSPARENCY SLOPE VS. TF AREA	51
APPENDIX F: HIGH WAVENUMBER TRANSPARENCY SLOPE VS. TF DEPTH.....	53
APPENDIX G: DEPTH OF THE 3RD VIBRATION BAND VS. CF SPECTRAL DEPTH	55
APPENDIX H: DEPTH OF THE 3RD VIBRATION BAND VS. TF AREA	57
APPENDIX I: DEPTH OF THE 3RD VIBRATION BAND VS. TF DEPTH	59
APPENDIX J: CF SPECTRAL DEPTH VS. TF AREA.....	61
APPENDIX K: CF SPECTRAL DEPTH VS. TF DEPTH	63
APPENDIX L: TF AREA VS. TF DEPTH	65
APPENDIX M: COMBINED TRENDLINE PLOTS - HIGH WAVENUMBER TRANSPARENCY SLOPE	67
APPENDIX N: COMBINED TRENDLINE PLOTS - TF AREA	69
APPENDIX O: COMBINED TRENDLINE PLOTS - TF DEPTH.....	71
APPENDIX P: COMBINED TRENDLINE PLOTS - CF SPECTRAL DEPTH	73
APPENDIX Q: COMBINED TRENDLINE PLOTS - DEPTH OF THE 3 RD VIBRATION BAND	75
APPENDIX R: COMBINED TRENDLINE PLOTS - DEPTH OF THE 6 TH VIBRATION BAND	77

APPENDIX S: COMBINED TRENDLINE PLOTS - DEPTH OF THE 9TH VIBRATION

BAND 79

LIST OF REFERENCES 81

LIST OF FIGURES

Figure 1: Typical TIR Spectrum with the Location of Important Spectral Features Marked.	6
Figure 2: Sample Particle Size Distributions	11
Figure 3: Images of Prepared Samples	14
Figure 4: Apparatus Used to Create Deposited Samples	17
Figure 5: Microscopic Images and Binarized Microscopic Images	20
Figure 6: Ambient Spectra with Varying Particle Size Distributions	21
Figure 7: Ambient Spectra with Varying Packing Styles	22
Figure 8: Select Surface Porosity Trendline Plots	32
Figure 9: Select Combined Surface Porosity Trendline Plots.....	33

LIST OF TABLES

Table 1: Particle Size Fractions by Weight Percentage for Lunar Particle Size Distributions	10
Table 2: Bulk Porosities and Surface Porosities with Associated Uncertainties	19
Table 3: Positions of All Five Distinct Spectral Features Across All Three Packing Styles (cm^{-1})	24
Table 4: Equations for the Spectral Feature Locations (cm^{-1})	26
Table 5: Measured Spectral Parameters for Variable Surface Porosity and Particle Size	28

1. INTRODUCTION

The Moon and other airless bodies of the Solar System are observed to have noticeably fine-particulate, porous (commonly known as "fairy castle" structure) regolith; due to several factors such as a weak gravitational field, the lack of an appreciable atmosphere, and relatively high electric fields present at the surface (Hapke and Van Horn, 1963; Carrier et al., 1991; Hapke, 1993). At the Apollo landing sites, the particle size distribution of the regolith was relatively well understood, due to the analyses of returned drive tubes and regolith samples (e.g., McKay et al., 1972). However, these particle size distributions may not be representative of the lunar surface as a whole as they originated from a small region of the lunar surface. Additionally, the porosity of the regolith was not measured in-situ by the Apollo astronauts, and it would have been impossible to maintain the porosities of any collected sample during its journey back to Earth. Thus, the in-situ regolith porosity was poorly constrained across the lunar surface (Hapke and Van Horn, 1963; Carrier et al., 1991). Recent work by Hapke and Sato (2015) estimated the porosity of the upper regolith near the location of the Apollo 16 lander using observations from the Kaguya Multiband Imager (MI) and the Lunar Reconnaissance Orbiter Narrow and Wide Angle Cameras (LROC NAC and WAC). Hapke and Sato (2015) estimated the porosity of the upper regolith in this region to be $83 \pm 3\%$, which was consistent with previous estimates in the 80 to 90% range (Hapke and Van Horn, 1963). With a better understanding of the regolith's porosity and particle size distribution across the lunar surface, we could effectively use remote sensing techniques like thermal infrared (TIR) spectroscopy to place better constraints on the compositional properties of the lunar surface.

Thermal IR spectroscopy ($\sim 2000 - 200 \text{ cm}^{-1}$ or $5 - 50 \text{ }\mu\text{m}$) is one of the most valuable tools we have to understand the composition of the upper hundreds of microns of a planet's regolith; however, there are several important hurdles to overcome before this tool could be utilized to its fullest potential. The TIR waveforms emitted from the surface of a body are altered by factors such as the albedo, composition, particle size, porosity, and near-surface thermal gradients in the regolith (e.g., Logan and Hunt, 1970; Logan et al., 1973; Henderson and Jakosky, 1994, 1997). Determining exactly how each of these factors modifies the TIR spectra collected via remote sensing is still an ongoing process (e.g., Donaldson Hanna et al., 2017; Shirley et al., 2018; Shirley and Glotch, 2019; Donaldson Hanna et al., 2021).

Additionally, it is challenging to compare remote sensing observations with laboratory measurements. While remote sensing observations of the lunar surface are prevalent, the spatial resolutions of these observations are far lower than the resolution of corresponding laboratory studies; the mixing scales of remote sensing observation and lab measurements are extremely different which can lead to issues interpreting global data sets (e.g., Donaldson Hanna et al., 2017). In-situ spectral measurements of the lunar surface and other airless bodies remain a critical link between laboratory measurements and remote sensing observations; without these in-situ measurements, uncertainties in mineralogical identification and their quantification will continue to exist.

Previous laboratory studies have characterized the effects of porosity on the TIR spectra of “fluffy” and “packed” silicate samples (e.g., Salisbury and Wald, 1992). As the porosity of a sample increases, the particles become separated by distances larger than the wavelengths of the TIR. At these higher porosities, the particles act as optically thin, volume scattering particles,

which scatter independently. This independent scattering results in less pronounced fundamental vibration bands (also known as reststrahlen bands) in the measured spectra. Other lab studies have also created highly porous samples for other purposes, such as reproducing electrostatic dust transport (Wang et al., 2016), and the formation of macroscopic dust aggregates during protoplanetary formation (Blum et al., 2006). Wang et al., (2016) used an electrostatic lofting chamber capable of mobilizing dust particles into highly porous structures resembling the observed features on asteroids, such as the "dust ponds" on near-Earth asteroid 433 Eros, and ballistically ejected silicate particles reminiscent of the lunar horizon glow phenomena.

To understand the properties of protoplanetary dust aggregates, Blum et al. (2006) designed an experiment in which individual silicate particles were lofted to assemble micron-sized dust particles into centimeter-sized, highly porous structures, reminiscent of the conditions during the early Solar System. They estimated that the bulk porosities produced in their samples were between 85% and 93%. Reflectance and emission spectra measured across the TIR portion of the electromagnetic spectrum of these highly porous structures suggested that increased porosity steepened the spectral slope shortward of the Christiansen feature (CF), a spectral feature of silicate minerals corresponding to where the real portion of the refractive index is equal to the refractive index of the ambient medium (e.g., Conel, 1969; Logan et al., 1973). From this point forward in the text the “spectral slope shortward of the Christiansen feature” will be referred to as the “high wavenumber transparency slope”.

Studies such as Salisbury and Wald (1992) left their porosities unmeasured, while studies such as Blum et al. (2006) calculated a sample’s bulk porosity using the volume of the sample cup and the average density of the particles. However, a sample’s bulk porosity is not responsible for

the changes in an emission spectrum measured via TIR spectroscopy. TIR measurements are sensitive to the porosity of the upper hundreds of microns (Logan et al., 1973; Henderson et al., 1996; Henderson and Jakosky, 1997), rather than the entire depth of a sample cup. Arnold et al. (2016) found that the surface layers (approximately the upper 100 μm) of a 10 mm silica sphere sample were nearly 50% more porous than the bottom millimeter of a 5 mm deep sample cup; this further supports the importance of surface porosity studies rather than bulk porosity studies. No study has yet to approximate the surface porosity of particulate samples and relate this to the observed TIR spectral changes.

Laboratory studies have also been conducted to characterize the effects of particle size on TIR spectra. An investigation of silicate minerals by Lyon (1964) determined that a reduction in particle size resulted in a corresponding decrease in the spectral contrast of the Christiansen feature and a decrease in the spectral contrast of the vibration bands. Recent work by Shirley and Glotch (2019) demonstrated that the positions of the vibration bands and the transparency feature (TF) did not shift as particle size changed, but the spectral contrast of the TF increased with reduced particle size. Their measurements did suggest that the Christiansen feature shifted with particle size; however, the degree of the shift was mineral dependent. In the spectra of most minerals in their study, notably forsterite (magnesium-rich olivine), the CF was observed to shift towards lower wavenumber with reduced particle size. Both Lyon (1964) and Shirley and Glotch (2019) analyzed individual particle size fractions, which are invaluable to understanding the relationship between particle size and TIR spectral features but were not reminiscent of the particle size distributions of the lunar regolith (King et al., 1971; 1972; Butler and King, 1973; Graf, 1993; Meyer, 2009).

For our investigation, we generated five particle size distributions, four of which were created to simulate returned Apollo lunar regolith particle size distributions, and the last was a purely $< 45\text{ }\mu\text{m}$ sample. Each of these five particle size distributions were then prepared with three different packing styles. All 15 of the prepared samples were then imaged and analyzed to estimate each sample's surface porosity. We then collected TIR emissivity spectra of the samples and characterized observed changes in TIR spectral features as particle size and surface porosity varied. The goal of this investigation was to determine if the spectral changes due to increased surface porosity could be uniquely distinguished from the spectral changes due to reduced particle size.

2. BACKGROUND

Minerals are composed of a series of repeating crystal lattice structures that vibrate at discrete frequencies. These structures absorb radiation at wavelengths identical to those vibrations (Estep-Barnes, 1977). For silicates, these fundamental vibration modes are due to the stretching and bending of Si-O bonds with energies that correspond to the TIR portion of the electromagnetic spectrum and appear as a series of minima within emissivity spectra (Figure 1). Because these vibration bands are caused by a mineral's unique crystal lattice structure, they could be used to uniquely identify the chemistry of that mineral (e.g., Rubens and Nichols, 1897; Lyon, 1964; Salisbury and Walter, 1989; Hamilton, 2000).

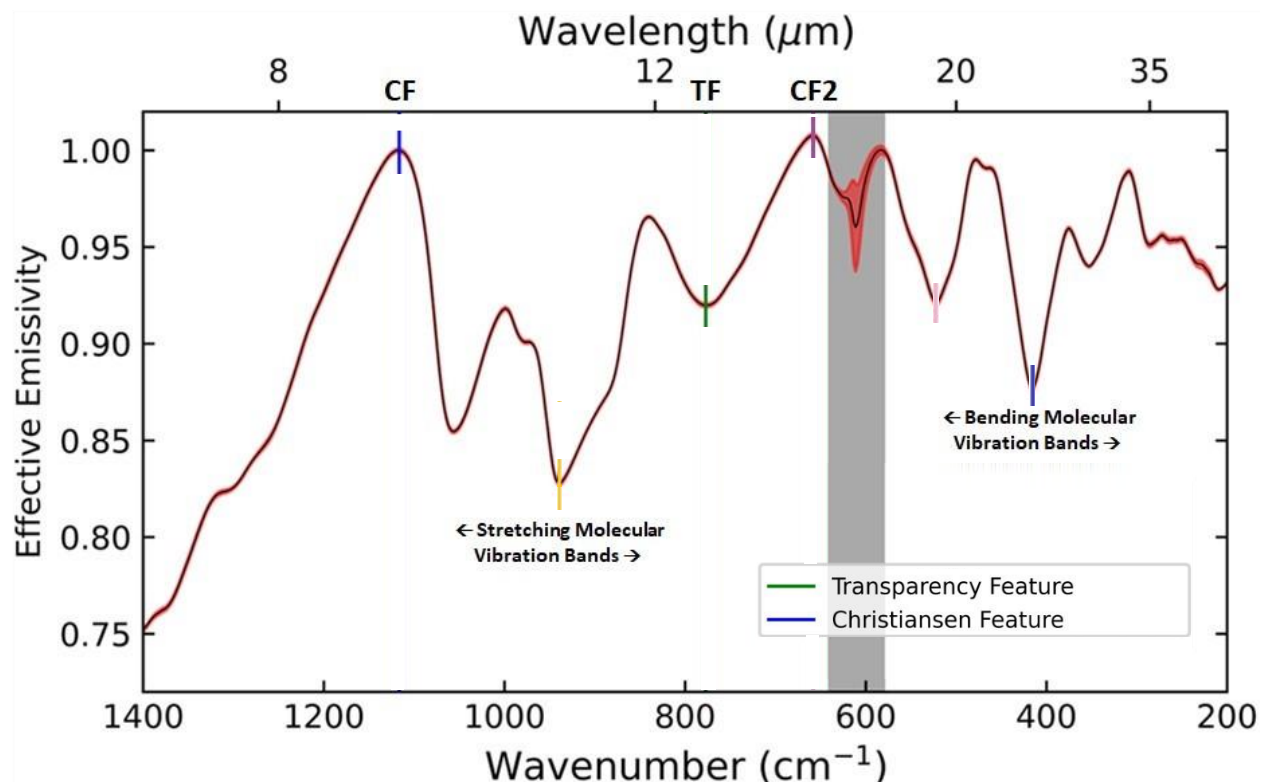


Figure 1: Typical TIR Spectrum with the Location of Important Spectral Features Marked.

From left to right: the Christiansen feature, the 3rd vibration band, the transparency feature, the 2nd Christiansen feature, the 6th vibration band, and the 9th vibration band.

At wavelengths shorter than the fundamental molecular vibration bands (Figure 1), the Christiansen feature appears as a maximum in emissivity spectra (e.g., Conel, 1969; Logan et al., 1973). A mineral's refractive index undergoes anomalous dispersion causing it to vary wildly just before (shorter wavelength) the vibration bands (e.g., Salisbury et al., 1992; Cooper et al., 2002). At some characteristic wavelength during this anomalous dispersion the real portion of a mineral's refractive index is equal to the refractive index of the ambient medium, which causes the observed peak in the TIR spectrum (e.g., Conel, 1969). The location of the CF is unique for each mineral allowing it to be used as a discriminator of mineral composition and bulk composition for a mixture of minerals (Conel, 1969).

Another important TIR spectral feature is the transparency feature. The TF is observed as a local minimum in a mineral's emissivity spectrum (Figure 1) and occurs between the mineral's stretching and bending vibration bands, typically between 11 and 13 μm (e.g., Salisbury et al. 1987; Salisbury and Walter, 1989; Cooper et al., 2002). The TF occurs when the wavelength of the incident radiation approaches the size of the scattering particles, resulting in volume scattering rather than surface scattering (e.g., Salisbury and Walter, 1989; Cooper et al., 2002). Thus, the TF only appears in TIR spectra when a mineral's particle size distribution is dominated by fine particulates, typically $< 63 \mu\text{m}$ for silicates (e.g., Salisbury and Walter, 1989). Because the TF is located between the stretching and bending vibration bands it shifts along with them as they move; thus, the location of the TF could also be an indicator of composition (e.g., Salisbury and Walter, 1989).

Increased porosity and reduced particle size both exhibit similar effects on the TIR spectra of particulate silicates; each result in decreased spectral contrast of the vibration bands and

increased spectral contrast of the TF (e.g., Lyon, 1964; Salisbury and Wald, 1992; Cooper et al., 2002). Low porosity samples behave similarly to a single large particle because the distances between the individual grains are small (Salisbury and Wald, 1992). As the porosity of a sample was increased the separation between particles also increases. When the particles are separated by distances larger than the wavelengths of TIR radiation; particles scatter independently, as optically thin, volume scattering particles (e.g., Salisbury and Wald, 1992). This volume scattering component increases with increased porosity leading to a reduction in the spectral contrast of the vibration bands (Salisbury and Wald, 1992).

In addition to their similar effects on TIR spectra, as particle size was reduced, electrostatic forces could create the aforementioned fairy castle structures described in Hapke and van Horn (1963). The critical particle size diameter required for these fairy castle structures to be created was roughly 15 μm for materials such as pulverized rock when prepared in atmospheric conditions (Hapke and van Horn, 1963). These highly porous structures are formed by van der Waals forces adhering particles into “bridges and branches” (Hapke and van Horn, 1963; Salisbury and Wald, 1992). This results in an intimate connection between porosity and particle size, which makes disentangling their effects on the TIR challenging.

3. METHODS AND ANALYSIS

3.1 Sample Production and Particle Size Analysis

We have chosen San Carlos olivine as our analog sample for this investigation as it has been well-characterized in the lab, particularly at TIR wavelengths (e.g., Hamilton, 2010). Our San Carlos olivine sample began as unpolished gem-quality crystals, each measuring a few mm across. The sample was sorted into three groups by visibly inspecting each crystal under an illuminated magnifying glass: pristine crystals, crystals with external impurities, and crystals with internal impurities. Olivine crystals with external inclusions were placed within a rock polisher for several weeks and then removed, cleaned, and re-sorted. All crystal materials that were free of any impurities were ground using a mortar and pestle and sieved into six particle size fractions: $< 45 \mu\text{m}$, $45 - 75 \mu\text{m}$, $75 - 125 \mu\text{m}$, $125 - 250 \mu\text{m}$, $250 - 500 \mu\text{m}$, and $500 - 1000 \mu\text{m}$. We created five different particle size distributions from those six particle size fractions.

Our first particle size distribution was composed solely of the $< 45 \mu\text{m}$ particle fraction, this size fraction was chosen because it was numerically dominated by fine particulates, which dominate TIR spectral signatures (e.g., Salisbury and Walter, 1987). We then created four particle size distributions to simulate the lunar regolith: mature mare, immature mare, mature highlands, and immature highlands. We gathered particle size distributions from the Lunar Sample Compendium of all well-characterized surface soil samples collected during the Apollo missions (King et al., 1971; 1972; Butler and King, 1973; Graf, 1993; Meyer, 2009). For our investigation, mature and immature lunar soils were separated by their concentrations of metallic nanophase iron (I_s) ratioed to their total abundance of iron oxide (FeO); such that immature lunar soils have an $I_s/\text{FeO} < 30$ and mature lunar soils have an $I_s/\text{FeO} > 60$ (Morris, 1976). Each of the four lunar

regolith simulants were calculated by averaging the particle size fractions from all lunar soils with documented particle size distributions listed in the Lunar Sample Compendium. Mare samples included regolith collected from the Apollo 11, 12, 14, 15, and 17 landing sites and highland samples included regolith collected from the Apollo 16 landing site. It should be noted that the immature highlands were only represented by a single surface soil sample. We simulated the immature mare, mature mare, immature highlands, and mature highlands by combining the six olivine particle size distributions in the weight fractions given in Table 1.

Table 1: Particle Size Fractions by Weight Percentage for Lunar Particle Size Distributions

Particle Size (μm)	Mature Mare	Mature Highlands	Immature Mare	Immature Highlands
500 - 1000	5.2%	7.9%	7.3%	11.9%
250 - 500	8.9%	11.1%	10.9%	16.6%
125 - 250	14.7%	15.1%	15.8%	16.9%
75 - 125	13.4%	12.4%	13.2%	11.2%
45 - 75	12.5%	11.0%	14.9%	11.2%
< 45	45.3%	42.5%	37.9%	32.3%

We measured the mean particle size of our < 45 μm sample and our four simulated lunar regolith samples using a CILAS Model 1190L Laser Particle Size Analyzer. Each measurement consumed 0.10 ± 0.005 g of material and roughly 10 ml of a mixture composed of deionized water and approximately 5% sodium hexametaphosphate ($NaPO_3$)₆, a dispersing agent added to prevent flocculation of the particles. Each of the lunar regolith simulants were measured twice, and the final particle size distribution was calculated by taking the average of each pair of measurements for each of the 80 particle size bins. The mean (μ), median, and standard deviation (σ) were then calculated across all 80 particle size bins for each of our regolith simulants. The average particle size distributions for each of our five lunar regolith simulants (< 45 μm , simulated mature mare,

simulated mature highlands, simulated immature mare, and simulated immature highlands) are presented as histograms in Figure 2.

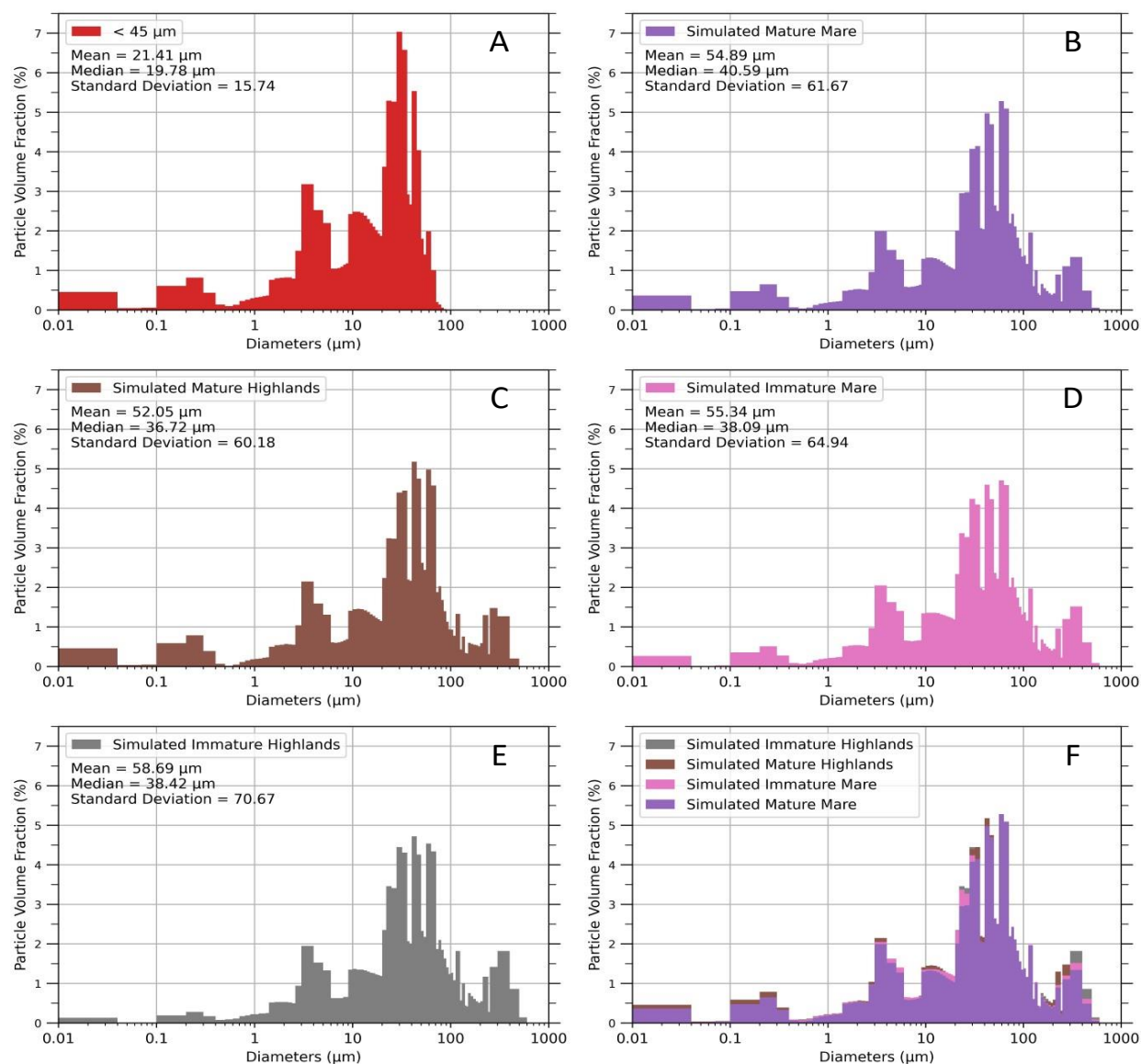


Figure 2: Sample Particle Size Distributions

Histogram plots showing the particle size distributions of the < 45 μm (A), simulated mature mare (B), simulated mature highlands (C), simulated immature mare (D), simulated immature highlands (E), and a stacked bar histogram displaying the four lunar particle size distributions together for reference (F).

We had intended to simulate the lunar soils as accurately as possible; however, the CILAS particle size analyzer suggested that our four lunar regolith simulants did not truly mimic their counterpart lunar soils. We know our lunar regolith simulants included material $> 700 \mu\text{m}$; however, the CILAS particle size analyzer did not accurately measure this size fraction (Figure 2). The reason for this apparent absence of large particles from our lunar regolith simulants may be due to the CILAS particle size analyzer itself. The CILAS particle size analyzer requires the particles to stay suspended in the solution for their diameters to be measured. When making particle size measurements of our samples without the magnetic stirrer and sonic vibrations turned on, larger particles immediately settled out of the solution and were not observed in the measurements. Although both were activated during all measurements presented in this paper, it was possible that the largest olivine particles may not have been suspended in the solution long enough to be measured by the particle size analyzer. Additional text corresponding to differences between our lunar regolith simulants and those tabulated in the Lunar Sample Compendium are discussed in A1.

Lastly, the mature highlands regolith simulant should have displayed an overall larger particle size than the mature mare regolith simulant sample; however, this was not what was measured. The CILAS particle size analyzer suggested that the mature highlands simulant was composed of 5% smaller material than the mature mare simulant (Figure 2). This inversion in the order of the particle size distributions of the mature highlands and the simulated mature mare simulants were further corroborated with TIR spectral measurements described later in this manuscript.

3.2 Sample Packing Methods

For each of our five simulants, we varied the porosity by filling the sample cup using three different methods (Figure 3). The packed, low porosity, (Figure 3A) method required filling the sample cup and then applying 88 to 108 N of force with a flat surface to the top of the sample to compress it. We then added more sample material, and we repeated until the sample could no longer be compressed. The leveled sample (Figure 3B) was our intermediate porosity technique. We gently poured each sample into the sample cup and leveled the surface by dragging a straight edge across the top of the sample. If any major voids were created during this process, additional material was gently poured in, and the process was repeated until the top of the sample was nearly uniform. However, as seen in Figure 3B, the surface of the leveled samples still displayed a higher topographical contrast than either sample made using the other methods. Next, we have our deposited sample (Figure 3C), which was the most porous sample we generated. We used an apparatus designed and constructed by Divspec that was attached to a Gilson Performer III sieve shaker and holds a 3-inch sieve to the side of the sieve shaker base (Figure 3). When the sieve shaker was turned on, a 75 μm sieve was shaken and its contents were slowly deposited in a sample cup placed beneath it on a separate table; thus, the stationary sample cup was relatively free from vibrations generated by the sieve shaker (a more detailed discussion of this is presented in Appendix B). We prevented air currents from disrupting the sample-making process with the inclusion of a Teflon cylinder directly below the open sieve, which enclosed the sample cup (Figure 4). The sieve was placed approximately 46 cm above the sample cup. This height was far enough above the sample cup for our olivine samples to reach terminal velocity, which ensured particle velocities were due to interactions with the column of air beneath. It should be noted that because our deposited samples were first passed through a 75 μm sieve, the targeted particle size

distribution of the deposited samples are different (0 – 75 μm) from that of the packed and leveled samples (0 – 1000 μm).

3.3 Sample Characterization

3.3.1 *Bulk Porosity Calculation*

We calculated the bulk porosity (Φ) for each sample following Equation 1:

$$\Phi = 1 - \frac{\rho_{bulk}}{\rho_{crystal}} \quad (1)$$

where ρ_{bulk} was the bulk density of the sample and $\rho_{crystal}$ was the crystal density of olivine.

The bulk density of the sample was calculated by measuring the mass of the sample in the sample cup and dividing it by the total volume of the sample cup. Uncertainties in the bulk porosities were calculated from the uncertainties for the measured dimensions of the sample cup (0.1 mm) and the uncertainties for the Mettler Toledo XPR204S electronic balance (0.0001 g).

The bulk porosities and their uncertainties for all 15 measurements are tabulated in the first column of Table 2.

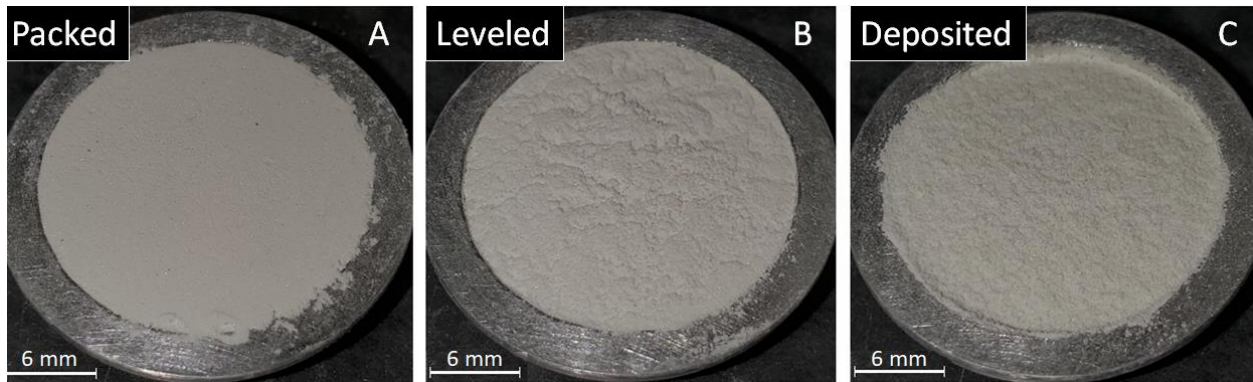


Figure 3: Images of Prepared Samples

Images of packed (A), leveled (B), and deposited (C) San Carlos olivine < 45 μm samples. Note the high topographical contrast of the leveled sample.

3.3.2 *Surface Porosity Calculation via Microscopic Imaging and Image Analysis*

We imaged our samples using a Dino-Lite Edge digital microscope at 225 times magnification (Figure 5). We tested several magnification levels and found that magnifications lower than 225X did not exhibit enough detail in the surface topography for our investigation. Higher magnifications, on the other hand, offer a different issue; any individual field of view had imaged an area much smaller than the sample cup. At these magnifications, each field of view varied from one another, and many images of the surface would need to be collected and analyzed to generate representative porosity estimates. In addition, at very high resolutions the microscopic imager had difficulty focusing on the highly variable topography, which resulted in large portions of our images being out of focus.

Our microscope images were processed (Figure 5) and analyzed using Python algorithms. First, we averaged each of the RGB bands to create a single grayscale image with pixel values ranging from 0 to 255. We then corrected the image from vignetting effects, caused by the incident microscope light not uniformly illuminating the entire sample. To remove this effect, we subtracted a Gaussian blur from each image, which effectively acted as dark frame subtraction. The resulting images had more uniform illumination across the sample surface (Figure 5A – C).

We analyzed the images using the geospatial image analysis software, ENVI. For our packed samples, we used the mean pixel value as the binarization threshold. For our leveled samples, we used the mean plus half of the standard deviation of the pixel value as the binarization threshold. For the deposited samples, we used the mean plus the standard deviation as the binarization threshold. Using these thresholds for each of the packing styles resulted in reproducible surface porosities. For each image, the pixel values that were less than our

binarization threshold value were converted to 0 (black), representing voids and those above our threshold value were converted to 255 (white), which represented the olivine particles (Figure 5D – F). We then calculated the ratio of black pixels to the total number of pixels in the image; this fraction represents our estimated surface porosity of the sample (see Table 2).

Uncertainties for our surface porosity estimations were determined from the difference in surface porosity generated from a single pixel value change, above and below, our binarization threshold. For example, if a binarization technique suggested a binarization threshold of 137, we then calculated the surface porosities using binarization thresholds of 136 and 138; this suggested an uncertainty of $\pm 3\%$ for that image. In general, our deposited samples displayed the smallest uncertainties (2% to 4%), while our packed (3% to 5%) and leveled samples (3% to 4%) displayed similar levels of uncertainty. All of our surface porosity estimations along with their corresponding uncertainties are listed in Table 2.

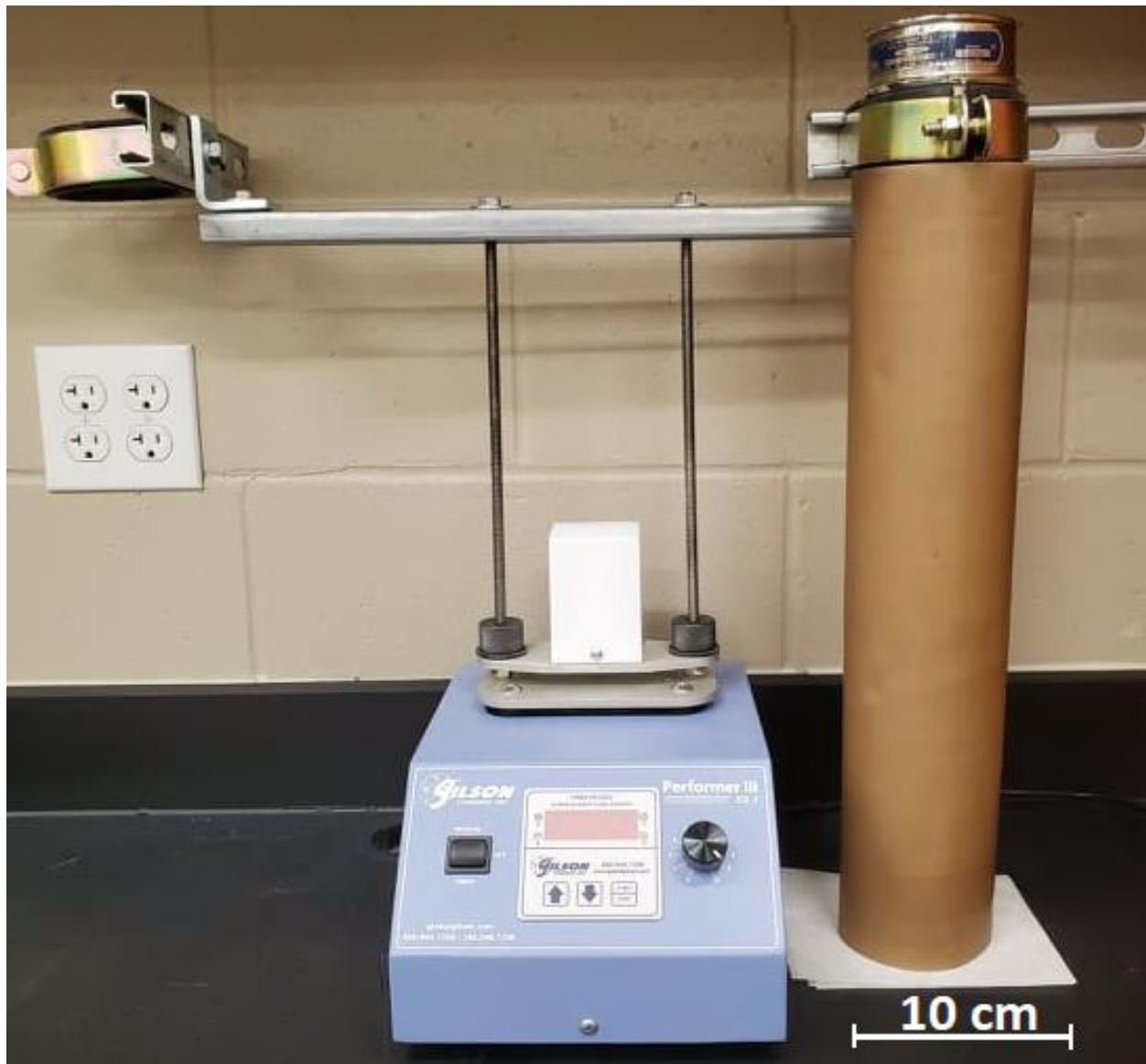


Figure 4: Apparatus Used to Create Deposited Samples

Divspec apparatus used to shake sieves off the main axis of the sieve shaker and deposit material into a sample cup. The sample cup sits directly below the sieve on the right side of the image at the bottom of the Teflon cylinder.

3.4 TIR Spectroscopy

After our samples were imaged, TIR emissivity measurements under ambient conditions were made using the Planetary Analogue Surface Chamber for Asteroid and Lunar Environments

(PASCALE). PASCALE was designed and built by the University of Oxford with the intended goal of simulating the near-surface conditions of airless bodies such as the Moon and asteroids (Donaldson Hanna et al., 2021). PASCALE is also capable of simulating the isothermal near-surface environment found on Earth (ambient conditions). Ambient conditions are achieved by backfilling the chamber with dry, spectrally inactive, nitrogen gas (N_2) to an atmospheric pressure of ~ 1000 mbar, holding the chamber at room temperature (~ 295 K), and heating the samples from below to 353 K (Donaldson Hanna et al., 2021).

Emitted radiation from the sample residing within PASCALE is passed through a cesium iodide (CsI) window and into the emission port of a Bruker Vertex 70 V Fourier Transform InfraRed (FTIR) spectrometer. For all measurements, a wideband beam splitter (T240-T/3) with a broadband deuterated triglycine sulfate (DTGS) detector was used for the range of ~ 2000 cm^{-1} to ~ 200 cm^{-1} (5 to 50 μm). For each spectral measurement, 250 scans at a velocity of 1.6 kHz and at a spectral resolution of 4 cm^{-1} are made. Across most of this spectral range, noise is low due to the number of scans and the chosen scanning velocity; however, there is increased noise in the region of low transmission caused by the FTIR's wide range beam splitter between 560 cm^{-1} and 620 cm^{-1} . We measure each sample three times, which allows for an estimate of the random measurement uncertainty (Donaldson Hanna et al., 2021).

Table 2: Bulk Porosities and Surface Porosities with Associated Uncertainties
Packed Samples

Sample Type	Bulk Porosity	Uncertainty	Estimated Surface Porosity	Uncertainty
$< 45 \mu m$	57%	$\pm 1\%$	58%	$\pm 5\%$
Simulated Mature Mare	43%	$\pm 1\%$	44%	$\pm 4\%$
Simulated Mature Highlands	43%	$\pm 1\%$	44%	$\pm 5\%$
Simulated Immature Mare	42%	$\pm 1\%$	44%	$\pm 4\%$
Simulated Immature Highlands	38%	$\pm 1\%$	43%	$\pm 3\%$

Leveled Samples

Sample Type	Bulk Porosity	Uncertainty	Estimated Surface Porosity	Uncertainty
$< 45 \mu m$	74%	$\pm 1\%$	75%	$\pm 4\%$
Simulated Mature Mare	66%	$\pm 1\%$	71%	$\pm 4\%$
Simulated Mature Highlands	67%	$\pm 1\%$	69%	$\pm 4\%$
Simulated Immature Mare	65%	$\pm 1\%$	71%	$\pm 4\%$
Simulated Immature Highlands	62%	$\pm 1\%$	71%	$+3\%$ -4%

Deposited Samples

Sample Type	Bulk Porosity	Uncertainty	Estimated Surface Porosity	Uncertainty
$< 45 \mu m$	82%	$\pm 0\%$	84%	$\pm 2\%$
Simulated Mature Mare	76%	$\pm 1\%$	80%	$\pm 3\%$
Simulated Mature Highlands	81%	$\pm 0\%$	79%	$\pm 3\%$
Simulated Immature Mare	76%	$\pm 1\%$	82%	$+3\%$ -4%
Simulated Immature Highlands	77%	$\pm 1\%$	80%	$\pm 3\%$

Three measurements are also collected at two temperatures bounding the sample measurement temperature, 340 K and 360 K, for both the calibration target and the black body target. The calibration target measurements are used to check the radiometric stability of the system and for any contamination in the system, and the measurements of the black body target are used to calibrate the sample measurements into effective emissivity (Ruff et al., 1997; Donaldson Hanna et al., 2021). Repeated spectral measurements of the black body and the samples allowed for the calculation of the uncertainties in the resulting effective emissivity spectra (Donaldson Hanna et al., 2021). The uncertainty in the effective emissivity (ignoring the large uncertainties caused by a region of low transmission caused by the FTIR's wide range beam

splitter) between 1400 cm^{-1} and 200 cm^{-1} was on average 0.0014 across all spectra. The average maximum uncertainty across all spectra was 0.0023 and the average minimum uncertainty across all spectra was 0.00064.

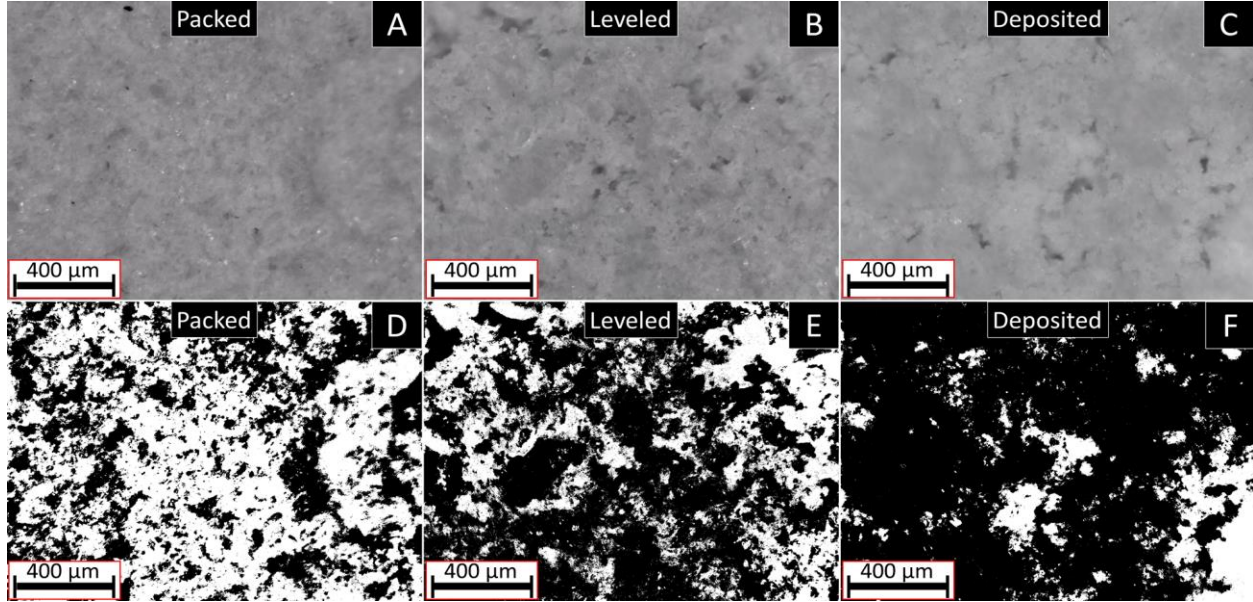


Figure 5: Microscopic Images and Binarized Microscopic Images

Across the top, we have our packed (A), leveled (B), and deposited (C) grayscale microscope images and along the bottom, we have our packed (D), leveled (E), and deposited (F) images after binarization using our pixel thresholding technique.

We identified seven diagnostic spectral features across the TIR (Table 4): the high wavenumber transparency slope (slope calculated between 1220 and $\sim 1120\text{ cm}^{-1}$), the spectral contrast of the CF, the depth of the TF, the area of the TF, and the depth of the 3rd, 6th, and 9th vibration bands (VB3, VB6, and VB9) as defined by Burns and Huggins (1972). The 3rd, 6th, and 9th vibration bands were chosen because they were the three most prominent vibration bands for olivine in the TIR. At the approximate location of each of our seven spectral features, we fit a fourth-order polynomial across the center of the region surrounding the local extremum of each feature (Table 2). The local extremum of the polynomial was taken as the position of the spectral

feature (Table 3). Due to our use of a polynomial fit, the position of a feature was capable of shifting by up to 2 cm^{-1} in wavenumber space. This uncertainty was similar to those achieved by Donaldson Hanna et al. (2012) and Bates et al. (2019).

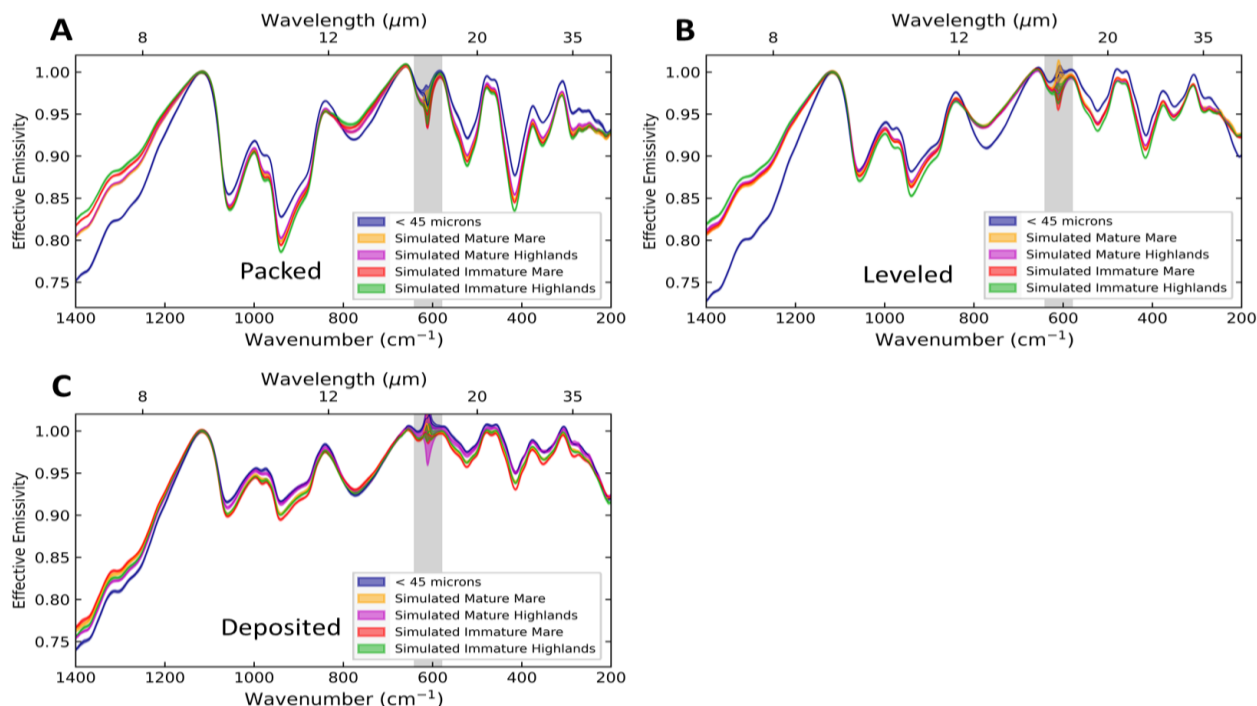


Figure 6: Ambient Spectra with Varying Particle Size Distributions

PASCALE ambient spectra of each porosity with different particle size distributions. (A) Our series of packed samples (low porosity), (B) our series of leveled samples (intermediate porosity), and Figure (C) our series of deposited samples (high porosity). The width of each line denotes the uncertainty in the measurement. The gray shaded region is a region of low transmission through the FTIR's wide range beam splitter.

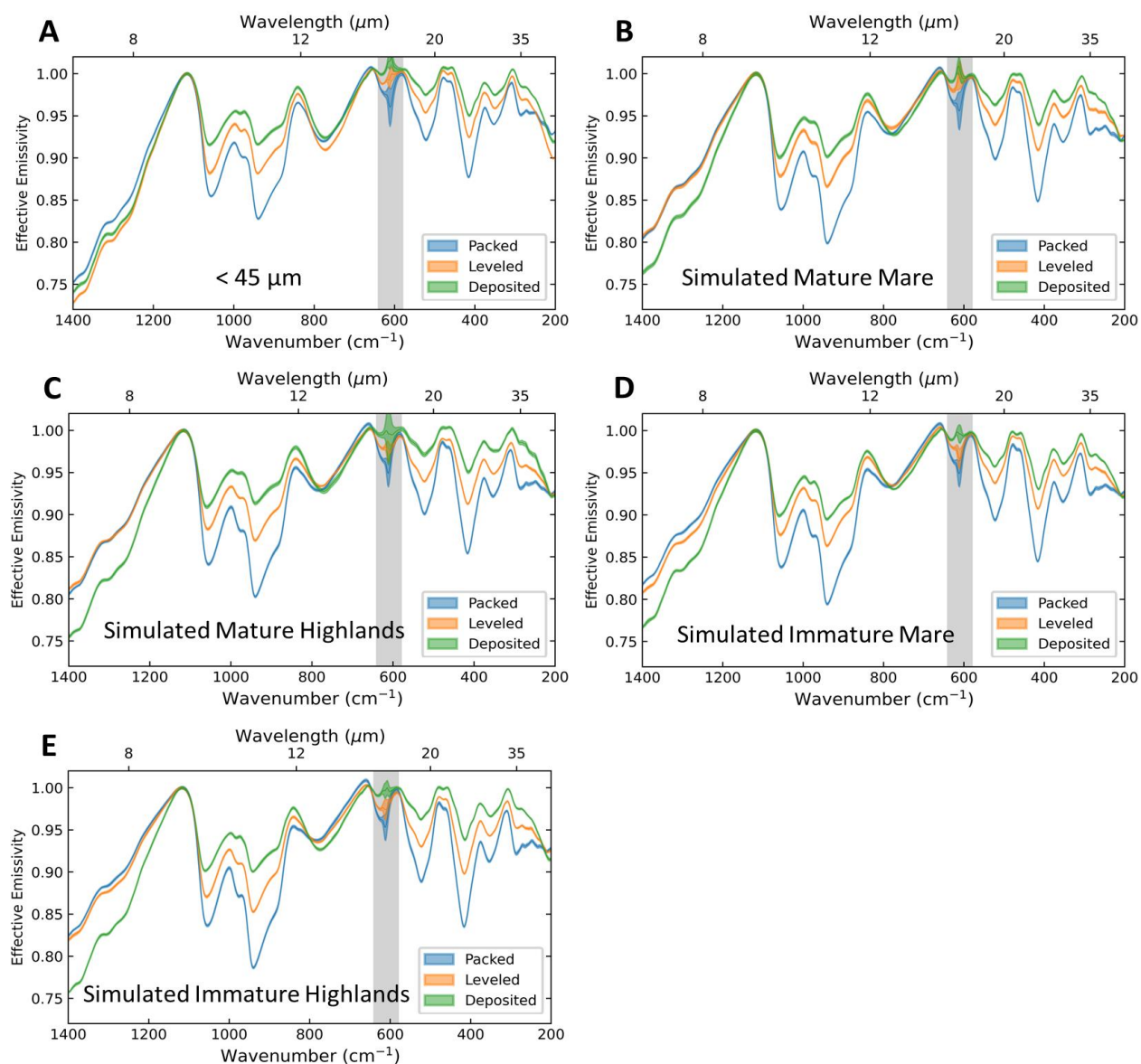


Figure 7: Ambient Spectra with Varying Packing Styles

PASCALE emissivity spectra of each sample with varying porosity (A) < 45 μm samples, (B) simulated mature mare samples, (C) simulated mature highlands samples, (D) simulated immature mare samples, and (E) simulated immature highlands samples. The width of each line denotes the uncertainty in the measurement. The gray shaded region is a region of low transmission through the FTIR's wide range beam splitter.

The spectral contrast of the CF was taken as the difference in effective emissivity between the CF and the minimum of the first vibration band (VB1; Table 4). The depth of the third vibration band was taken as the difference in effective emissivity between the CF and third vibration band (Table 4). The depths of the sixth and ninth vibration bands were taken as the difference between their respective effective emissivities and the effective emissivity maximum of the secondary CF ($\sim 660 \text{ cm}^{-1}$ or $\sim 15 \text{ }\mu\text{m}$) (Table 4). The depth of the TF was determined by fitting a continuum across the maxima on either side of the TF and measuring the difference in effective emissivity between the TF and the continuum at the same wavenumber (Table 4). For spectral area calculations, a fourth-order polynomial was used to smooth out the data and to interpolate between the measurements, and a continuum was fit between the local extrema of the polynomial on either side of the central feature location. We then calculated the area bound between the continuum and the polynomial (Table 4).

The uncertainties in effective emissivity were generated by calibrating the measurements made by PASCALE and are given as the standard deviation of each measurement. The uncertainties in the effective emissivity measurements were plotted along with the spectral measurements and appear as a light outline surrounding our curves (Figure 6 and Figure 7). This effective emissivity uncertainty was also used in our analysis of the spectral features to determine the final uncertainty for each spectral feature.

Table 3: Positions of All Five Distinct Spectral Features Across All Three Packing Styles (cm⁻¹)
Packed Samples

Spectral Feature	< 45 μ m	Sim. Mature Mare	Sim. Mature Highlands	Sim. Immature Mare	Sim. Immature Highlands
CF	1118	1118	1116	1116	1117
TF	777	783	780	780	784
VB3	939	939	939	939	939
VB6	523	522	522	523	523
VB9	417	416	417	416	417

Leveled Samples

Spectral Feature	< 45 μ m	Sim. Mature Mare	Sim. Mature Highlands	Sim. Immature Mare	Sim. Immature Highlands
CF	1117	1116	1119	1117	1117
TF	772	779	778	779	780
VB3	941	939	939	939	939
VB6	523	523	523	523	523
VB9	414	416	415	415	415

Deposited Samples

Spectral Feature	< 45 μ m	Sim. Mature Mare	Sim. Mature Highlands	Sim. Immature Mare	Sim. Immature Highlands
CF	1116	1116	1116	1116	1117
TF	773	773	772	775	775
VB3	941	940	939	941	941
VB6	523	523	523	524	524
VB9	415	414	415	415	415

We tracked how each of our spectral features were modified in response to changes in particle size (Figure 6) and surface porosity (Figure 7), which resulted in 245 sets of data for variable porosity and 147 sets of data for variable particle size. Each set was fit with a linear trendline, and an R-squared value was calculated. We then plotted these changes for each feature and compared them to every other feature (A3 – A12). In Figure 8 we present six different feature comparisons for several different particle size distributions, surface porosities, spectral features, and a range of R-squared values. For each set of feature comparisons, there were a total of eight different plots, three for variable porosity and five for variable particle size; each of these trendlines were then plotted on a single figure, resulting in a total of 49 combined trendline plots (Figures A13 – A19). Figure 9 presents two different trendline plots which displayed higher R-squared values but also some of the lowest correlations between surface porosity and particle size

trendlines, which would represent our best-case scenario to disentangle the effects of surface porosity from those of particle size.

4. RESULTS

Table 4: Equations for the Spectral Feature Locations (cm⁻¹)

Spectral Features	Location
High Wavenumber Transparency Slope	$\frac{E(1220) - E(\text{CF})}{1220 - W(\text{CF})}$
Spectral Contrast of the CF	$E(\text{CF}) - E(\text{VB1})$
Depth of the VB3	$E(\text{CF}) - E(\text{VB3})$
Depth of the TF	$E(\text{Continuum}) - E(\text{TF})$
Area of the TF	$\sum_{n=W(658)}^{W(841)} (E(\text{Continuum}) - E(\text{TF}))$
Depth of the VB6	$E(\text{CF2}) - E(\text{VB6})$
Depth of the VB9	$E(\text{CF2}) - E(\text{VB9})$

Note. E = emissivity; W = wavenumber; VB# = vibrational band number; E(Continuum) = hypothetical emissivity of a straight line connecting the two maxima on either side of the TF.

4.1 Surface Porosity Estimations

We used our binarization thresholding technique to estimate the surface porosities for each sample prepared with the three different packing methods. We found that the surface porosities were, on average, 3% higher than their measured bulk porosity counterparts (Table 2). Only 1 of the 15 measurements displayed a bulk porosity (81%) higher than its corresponding surface porosity (79%), and this difference was within the corresponding uncertainty of $\pm 3\%$ (Table 2). The surface porosity uncertainties were determined based on the location of our binarization threshold choices and thus, changed with the packing style. The estimated surface porosities of our

deposited samples of 79% to 84% are similar to porosities of the lunar regolith near the Apollo landing sites at approximately 80% to 90% (e.g., Hapke and Van Horn, 1963; Hapke and Sato, 2015).

4.2 Observed TIR Spectral Changes due to Surface Porosity

As surface porosity increased in each of our particle size distributions, we observed little to no shift in the position of most of the spectral features, as most shifts between packing styles lie within our wavenumber uncertainty of 2 cm^{-1} (Table 5). However, as surface porosity increased, we observed a shift in the position of the TF towards lower wavenumbers (Table 3). The TFs for the $< 45 \text{ }\mu\text{m}$, simulated mature mare, and simulated immature highlands spectra shifted to lower wavenumbers when we increased the surface porosity from the packed to the leveled samples. The spectra of the simulated mature highlands and simulated immature mare displayed no shifts in the TF, as both were within the uncertainty (Table 3). When the porosities of the samples were increased further from leveled to deposited, we saw a continued shift of the TF towards lower wavenumbers in the spectra of all four of the simulated lunar particle size lunar regolith simulants. This observed behavior of the TF agreed with previous investigations (e.g., Salisbury and Eastes, 1985).

Surface porosity had more of an effect on the shape and contrast of the spectral features than on their positions. For the high wavenumber transparency slope, we observed a minor increase in the slope between the packed and leveled spectra across all samples, with a 10% average increase in slope (Table 5). A larger increase in slope between the leveled and deposited spectra was observed for the four lunar regolith simulants with an average of a 39% increase in slope

(Table 5). The $< 45 \mu\text{m}$ spectra displayed essentially no change for the high wavenumber transparency slope between the leveled and the deposited spectra.

Table 5: Measured Spectral Parameters for Variable Surface Porosity and Particle Size

Packed Samples					
Spectral Feature	$< 45 \mu\text{m}$	Sim. Mature Mare	Sim. Mature Highlands	Sim. Immature Mare	Sim. Immature Highlands
High Wavenumber Transparency Slope	0.000090	0.000065	0.000065	0.000059	0.000056
Spectral Depth of the TF	0.060	0.042	0.044	0.036	0.033
Spectral Area of the TF	5.8	4.1	4.2	3.5	3.2
Spectral Contrast of the CF	0.145	0.161	0.159	0.162	0.164
Depth of VB3	0.172	0.201	0.197	0.206	0.214
Depth of VB6	0.086	0.109	0.107	0.115	0.121
Depth of VB9	0.130	0.159	0.154	0.163	0.174
Leveled Samples					
Spectral Feature	$< 45 \mu\text{m}$	Sim. Mature Mare	Sim. Mature Highlands	Sim. Immature Mare	Sim. Immature Highlands
High Wavenumber Transparency Slope	0.000106	0.000068	0.000066	0.000068	0.000062
Spectral Depth of the TF	0.077	0.044	0.044	0.045	0.043
Spectral Area of the TF	7.6	4.3	4.3	4.4	4.1
Spectral Contrast of the CF	0.118	0.121	0.117	0.123	0.129
Depth of VB3	0.118	0.134	0.130	0.136	0.147
Depth of VB6	0.051	0.064	0.062	0.066	0.073
Depth of VB9	0.081	0.094	0.089	0.096	0.105
Deposited Samples					
Spectral Feature	$< 45 \mu\text{m}$	Sim. Mature Mare	Sim. Mature Highlands	Sim. Immature Mare	Sim. Immature Highlands
High Wavenumber Transparency Slope	0.000104	0.000090	0.000095	0.000088	0.000093
Spectral Depth of the TF	0.068	0.058	0.061	0.054	0.059
Spectral Area of the TF	6.8	5.6	6.0	5.3	5.9
Spectral Contrast of the CF	0.084	0.099	0.091	0.101	0.098
Depth of VB3	0.084	0.098	0.087	0.105	0.099
Depth of VB6	0.030	0.038	0.032	0.044	0.039
Depth of VB9	0.055	0.062	0.052	0.071	0.063

The depth and area of the TF increased for the $< 45 \mu\text{m}$, the simulated immature mare, and the simulated immature highlands spectra, at roughly 28% each (Table 5). The simulated mature mare and simulated mature highlands spectra both displayed negligible increases in the depth and area of the TF (Table 5). Increasing the surface porosity further from the leveled to the deposited packing style, all four simulated lunar spectra displayed an increased depth of the TF and area of the TF. The average increase in the depth and area of the TF for the lunar regolith simulant spectra was roughly 32% and 33%, respectively. The spectrum of the $< 45 \mu\text{m}$ sample behaved differently

than the lunar regolith simulant spectra, it displayed a decreased depth of the TF by 12% and decreased the area of the TF by 11% (Table 5).

The contrast of the CF and the vibration bands all displayed similar behaviors to each other; increased surface porosity resulted in reduced contrast for all four spectral features (Table 3). This behavior was observed for the spectra of all five particle size distributions (Table 5). From the packed to the leveled spectra, there was an average reduction in contrast of 24% for the CF and 38% for the vibration bands. The increased porosity from the leveled to the deposited spectra displayed similar reductions in contrast; we observed an average reduction in contrast of 22% for the CF and 35% for the vibration bands. These observations of reduced contrast with increased porosity agree with previous investigations such as those by Salisbury and Eastes (1985) and Salisbury and Wald (1992).

Relationships between different spectral features became more apparent once data was plotted against one another. Nearly all the data points on our surface porosity trendlines (Figure A, Figure 8C, Figure 8E, Figures A3 – A12) are in order of surface porosity, either increased surface porosity (Figure 8E) or decreased surface porosity (Figure 8A). This was true for all our surface porosity trendlines except those including the $< 45 \mu\text{m}$ TF depth, $< 45 \mu\text{m}$ TF area, and $< 45 \mu\text{m}$ high wavenumber transparency slope (Table 5, Figure 8C, Figures A3 – A12). All three of these features displayed different behavior with their leveled samples displaying larger values than that of their deposited counterparts. This was counterintuitive as all other features across all packing styles displayed the opposite behavior (Table 3). The trendlines that included those features also had significantly lower R-squared values compared to the other surface porosity trendlines (Figures A3 – A19), suggesting lower confidence in those results.

4.3 Observed TIR Spectral Changes due to Particle Size

As the average particle size decreased, we observed negligible change in the position of the spectral features as most changes in position were within the 2 cm^{-1} uncertainties (Table 3). The only possible outlier was the position of the TF. The TF position was identified at 777 cm^{-1} for the packed $< 45\text{ }\mu\text{m}$ spectrum, while the TFs in the spectra of the packed lunar regolith simulants were identified at higher wavenumbers, 780 to 784 cm^{-1} (Table 3). The shift in TF position between the $< 45\text{ }\mu\text{m}$ spectrum and the lunar regolith simulant spectra was real as it was larger than the uncertainty in the TF position; however, the shift in position between the lunar regolith simulant spectra was inconsistent with particle size. Our two particle size endmembers of the lunar regolith simulants, the simulated immature highlands spectrum and the simulated mature mare spectrum, displayed higher wavenumber TF positions than the two intermediate particle size spectra. For the leveled $< 45\text{ }\mu\text{m}$ spectrum, we observed the TF position at 772 cm^{-1} while the lunar regolith simulant spectra occurred between 778 cm^{-1} and 780 cm^{-1} . Once again, the shift of the TF between the $< 45\text{ }\mu\text{m}$ spectrum and the lunar regolith simulant spectra were greater than the uncertainty and the shift in TF position between the lunar regolith simulant spectra were negligible (Table 3). Recent work by Shirley and Glotch (2019) suggested that the TF position should not shift with particle size, contrary to what was observed during our investigation of the packed and leveled samples. For the deposited spectra, the position of the TF did not change, with all TFs between 772 cm^{-1} and 775 cm^{-1} (Table 3), which was within our uncertainties and agreed with the work by Shirley and Glotch (2019).

Particle size had a greater effect on the shape and contrast of the spectral features than on their position. For all three of our packing styles, we observed an increase in the high wavenumber

transparency slope with reduced particle size. The $< 45 \mu\text{m}$ spectra consistently displayed the largest slope amongst the five particle size distributions while the simulated immature highlands spectra displayed the shallowest slope for the packed and leveled samples and the simulated immature mare displayed the shallowest slope for the deposited sample. The high wavenumber transparency slope has been explored by Ruff and Christensen (2002) for the purposes of TIR spectroscopy on the Martian surface. The average emissivity in the 1350 to 1400 cm^{-1} spectral region was used as a “dust cover index” to estimate the abundance of dust covering regions of interest on the Martian surface (Ruff and Christensen, 2002). A lower dust cover index value was indicative of a steeper high wavenumber transparency slope and suggests a greater abundance of fine ($< 63 \mu\text{m}$) particles. This increase in the high wavenumber transparency slope with reduced particle size agrees with the general trends observed for our spectra of packed and leveled samples. This trend did not continue with the deposited spectra; this may be explained by the fact that we reduced the particle size distributions of the lunar regolith simulants by using the $< 75 \mu\text{m}$ sieve to create the deposited samples. This reduction in particle size resulted in similar particle size distributions between the $< 45 \mu\text{m}$ sample and the four lunar regolith simulants.

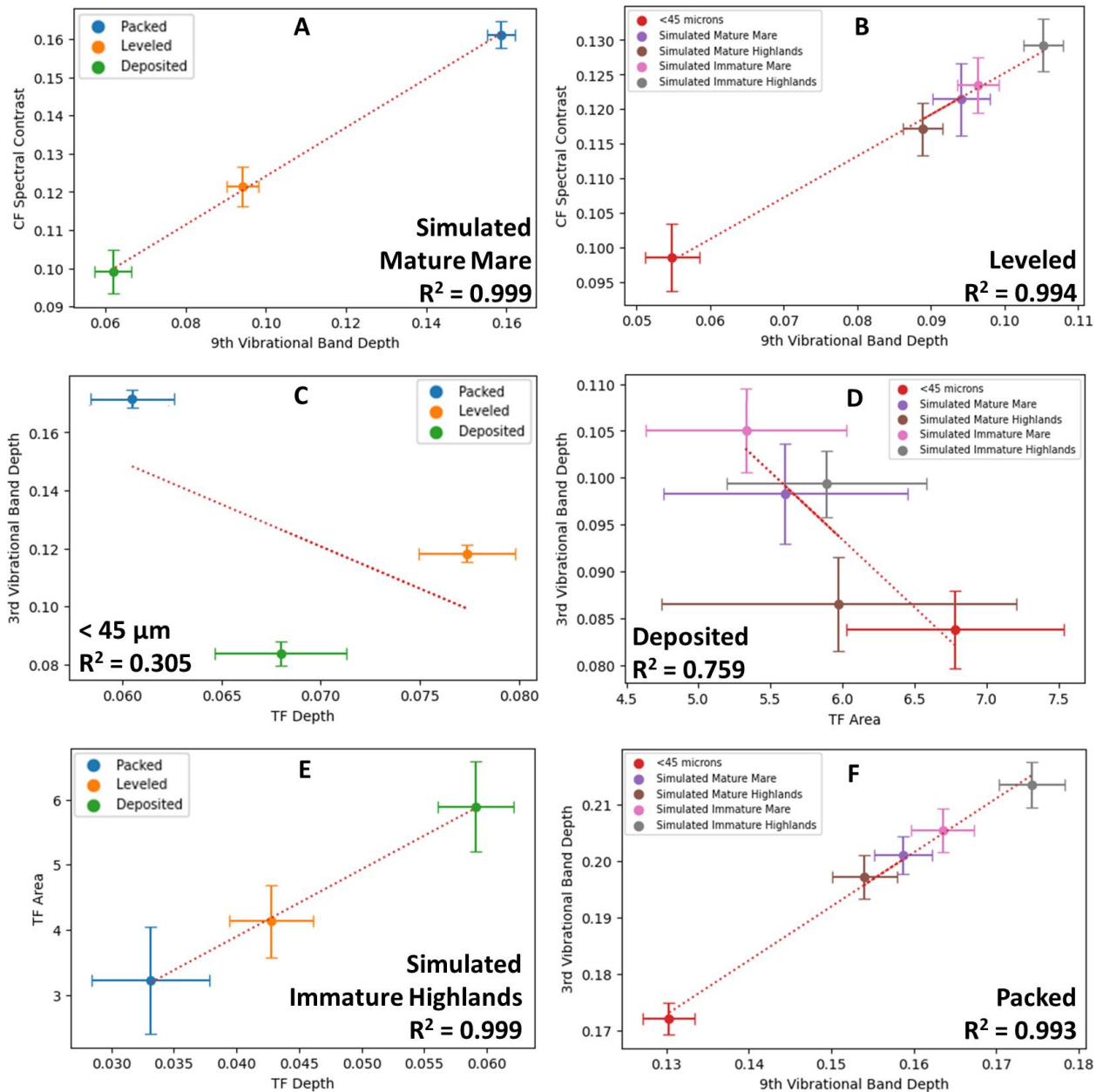


Figure 8: Select Surface Porosity Trendline Plots

Here we compared how several different spectral features changed compared to other features with either variable porosity or particle size. Note that we have higher porosities (or reduced particle size) towards the bottom left and lower porosities (or larger particle size) towards the upper right.

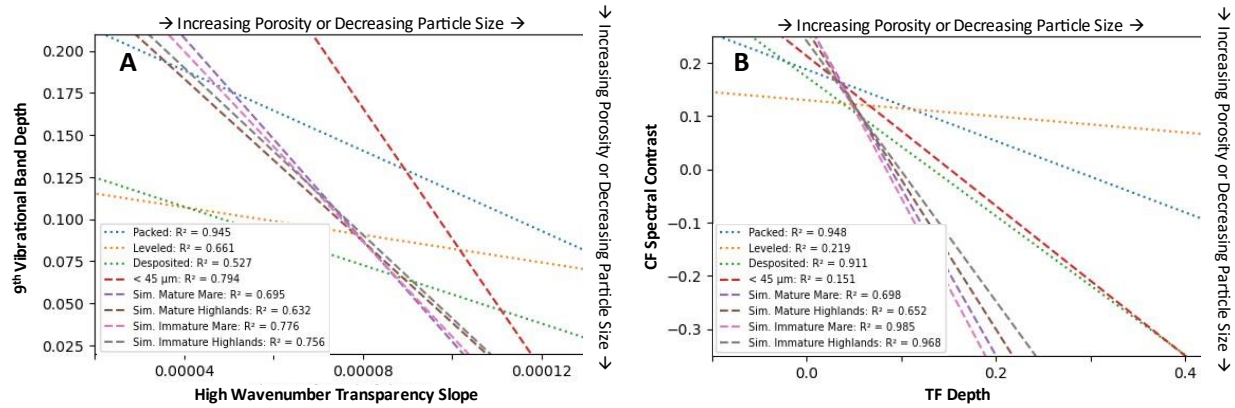


Figure 9: Select Combined Surface Porosity Trendline Plots

Each trendline on these figures represents a series of data points comparing two spectral features. In (A) we are comparing the depth of the 9th vibration band to the high wavenumber transparency slope and in (B) we are comparing the spectral contrast of the CF to the depth of the TF. Trendlines representing variable porosity samples are dotted, while trendlines representing variable particle size are dashed. Note that all trendlines in each figure have the same directionality.

We observed a relationship between reduced particle size and increased TF depth and TF area for the spectra of the packed and leveled samples. For both the packed and the leveled < 45 μm spectra, we observed a greater TF depth and a larger TF area than any of the lunar regolith simulant spectra (Table 5, Figure 7A, Figure 7B). Additionally, the spectra of the simulant with the largest average particle size, the simulated immature highlands, displayed the smallest contrast and area of the TF for both the packed and leveled spectra (Table 5, Figure 7A, Figure 7B). For the spectra of the deposited samples, the < 45 μm spectrum displayed the greatest TF depth and TF area; however, there was no trend between the four deposited lunar regolith simulant spectra with increased particle size. For the deposited spectra, the observed differences between the < 45 μm spectrum and the lunar regolith simulant spectra have been reduced (Table 5).

The depth of the vibration bands along with the contrast of the CF were observed to be weakest in the < 45 μm spectra for all packing styles, with a single exception, the 9th vibration band in the deposited sample (Table 5). The deposited simulated mature highlands spectra

displayed a shallower 9th vibration band than the deposited < 45 μm spectra (Table 5). Amongst lunar regolith simulant spectra, the trends between particle size and the contrast of the CF were negligible for all three packing styles (Table 5). The observed decrease in contrast of the vibration bands and the CF with reduced particle size between the < 45 μm spectra and the lunar regolith simulant spectra agreed with observations in previous studies, such as those conducted by Lyon (1964) and by Shirley and Glotch (2019).

4.4 Differences Between Surface Porosity and Particle Size

Changes in surface porosity and particle size resulted in similar changes in our spectra; however, there were a few observed differences worth noting (Table 3). Although most of the spectral features did not shift in position, we observed the TF shift in position as a function of surface porosity. As surface porosity increased the TF shifted towards shorter wavenumbers for all five lunar regolith simulants, except when increasing surface porosity from the leveled to the deposited < 45 μm spectra (Table 3). The shift of the TF due to surface porosity and not particle size suggests that the location of the TF could be used to disentangle their effects and help discriminate between varying surface porosities.

We also observed greater changes in the contrast of spectral features due to surface porosity than to particle size (Table 5). Ignoring the spectra of the < 45 μm samples, the average change in the high wavenumber transparency slope was 3.9 times greater for surface porosity changes than for particle size changes. For the depth of the TF, the surface porosity effects were 2.8 times larger, and the area of the TF displayed a change 3.0 times larger. We observed a 7.1 times increase in contrast of the CF due to increased surface porosity than from reduced particle size. The vibration

bands were observed to change by 5.2 to 6.0 times more for increased surface porosity than for reduced particle size. All four lunar regolith simulants included a sizable $< 45 \mu\text{m}$ component (32.3% to 45.3%) and this abundance of the $< 45 \mu\text{m}$ particle size fraction increased when we created our deposited samples (71.8% to 79.4%) using the $75 \mu\text{m}$ sieve on the lunar regolith simulants. It was known that fines ($< 5 \mu\text{m}$) numerically dominate the $< 45 \mu\text{m}$ sample when ground and sieved (e.g., Rowan and Becker, 1971; Salisbury and Walter, 1987). When fines numerically dominate a sample, they also dominate the TIR spectrum; thus, the $< 45 \mu\text{m}$ particle size fraction dominates the TIR spectra of particulate materials (e.g., Salisbury and Walter, 1987).

5. DISCUSSION

5.1 Porosity Estimations and Uncertainties

Surface porosity estimations were overall larger than their corresponding measured bulk porosities; this suggested porosity decreased with depth, a result that agreed with previous investigations conducted by Arnold et al. (2016). For each packing style, we observed some variation between the estimated surface porosities and the measured bulk porosities. The packed samples had the most similar values for their bulk and surface porosities. The similarity between the packed bulk porosity measurements and the packed surface porosity estimations is most likely caused by the act of compaction; as we packed the samples, any increased surface porosities would be compressed into the rest of the sample, which resulted in a more uniform porosity with depth. The leveled samples had the largest difference between the estimated surface porosities and the measured bulk porosities. These larger differences may be explained by the rough surface topography of the leveled samples generated when dragging a straight edge across the sample (Figure 3B). When dragging the straight edge across the sample, larger voids were created increasing the sample's surface porosity. While we tried to limit these larger voids by adding additional sample material to the sample cup and re-leveling the sample, these voids were unavoidable. The average difference between surface porosity estimations and the bulk porosity measurements for the deposited samples was greater than the packed samples but less than those of the leveled samples. Due to the low porosities, and correspondingly low masses of the deposited samples, less compaction of the samples was to be expected. In addition, the deposited samples had truncated particle size distributions; this lack of particles larger than 75 μm would further reduce any compaction from higher energy impacts during the deposition process (see Appendix

B). Together, these would suggest that the highly porous surface layers would not be significantly more porous than the bulk porosity, which was consistent with our observations.

5.2 Unexpected Behavior due to Surface Porosity Spectral Effects

Not all our variable particle size spectral measurements agreed with previous observations and many of these differences can be explained by changes in surface porosity. For the packed spectral measurements, we did not observe any shifts of the TF with particle size for the four lunar regolith simulants; however, we observed the TF in the $< 45 \mu\text{m}$ spectrum at a lower wavenumber than that of the lunar regolith simulants. This shift towards higher wavenumber with increased particle size was not observed by Vincent and Hunt (1968) or Shirley and Glotch (2019). Our observations lead us to believe that these effects could be explained by surface porosity dominating the effects of particle size; Salisbury and Eastes (1985) determined that decreased porosity resulted in a corresponding shift of spectral features towards higher wavenumbers. Although the packing styles for the four lunar regolith simulants were identical to that performed on the $< 45 \mu\text{m}$ sample, the packed lunar regolith simulants had an estimated average surface porosity of 44%, while the packed $< 45 \mu\text{m}$ sample had an estimated surface porosity of 58% (Table 2). Thus, the lunar regolith simulants have both larger particle sizes (Table 1, Figure 2) and reduced surface porosities (Table 2) than the $< 45 \mu\text{m}$ sample, the latter of which can lead to the changes we observed in the position of the TF (Salisbury and Eastes, 1985). However, our observations from our other two packing styles appear to contradict the surface porosity domination hypothesis; more lab measurements are necessary before we can conclude whether differences in surface porosity caused the differences amongst the variable particle size spectra. The position of the TF for the

leveled lunar regolith simulants had no observable relationship with particle size; however, we did see a shift in wavenumber between the $< 45 \mu\text{m}$ spectrum and the lunar regolith simulant spectra. The shift of the TF towards higher wavenumbers (7 cm^{-1}) for the leveled spectra was more difficult to explain than for the packed spectra. The estimated average surface porosity of the leveled lunar regolith simulants (71%) was similar to that of the estimated leveled surface porosity of the $< 45 \mu\text{m}$ sample (75%). Although particle size should have no effect on the TF position, it has not yet been demonstrated that a change in surface porosity of 4% was significant enough to shift the TF position by an appreciable amount. For the deposited samples the estimated surface porosity of the $< 45 \mu\text{m}$ sample (84%) and the lunar regolith simulants (80%) also differ by 4%; however, the effects due to surface porosity are not observed. For the deposited spectra we observed essentially no change in the position of the TF (Table 3); these results agreed with that of Vincent and Hunt (1968) and Shirley and Glotch (2019). This suggested that the effects due to particle size had a negligible effect on the position of the TF, but the position of the TF may shift due to changes in surface porosity.

5.3 Future Investigations

For future investigations to better disentangle the spectral effects due to surface porosity and particle size, several steps could be taken to reduce the challenges in interpreting spectral measurements. The initial step in this investigation was to reproduce particle size distributions of well-characterized lunar samples by grinding and sieving multiple particle size fractions and then combining them in the appropriate abundances. Unfortunately, we found it was difficult to accurately simulate the particle size distributions found in the lunar regolith due to the natural way

regolith breaks down on the lunar surface using the typical grinding and sieving techniques used in most laboratory investigations. We found that the act of grinding and sieving particle size fractions and then combining those fractions created more fine particles than were measured in the returned lunar regolith samples we were trying to simulate (Figure A1). If more accurate particle size distributions are needed in future investigations, additional techniques for creating particle size distributions will need to be investigated.

There was a large difference in the estimated surface porosity between the packed $< 45 \mu\text{m}$ sample (58%) and the packed lunar regolith simulants (43% to 44%). This difference could be minimized if the lunar regolith simulants were packed with less force to resemble the porosity of the $< 45 \mu\text{m}$ samples more closely. If the surface porosity of each packing style was more consistent, any spectral differences due to surface porosity would be eliminated, and any remaining differences in spectral behavior between packing styles could be attributed solely to particle size. Another issue occurred with the creation of our simulated lunar particle size distributions. We were unable to create high surface porosity samples via the deposition method without truncating the particle sizes of our lunar regolith simulants. The deposited lunar regolith simulants were reduced in particle size from roughly 0 to 1000 μm to 0 to 75 μm (see Appendix B). This reduction in particle size made comparisons between the leveled and deposited measurements challenging as any spectral changes could be due to either increased surface porosity or the truncated particle size distributions. In the future, a new technique will be needed to replace the deposition method used in this investigation so that the particle sizes and the surface porosities could be created more consistently for their spectral effects to be properly disentangled.

This investigation used the mineral olivine for all our measurements as olivine displays strong TIR spectral features and has been studied in this spectral region by past investigations (e.g., Salisbury et al., 1991; Clark et al., 2007; Hamilton, 2010; Kokaly et al., 2017), and was a silicate mineral found within lunar lithologies. However, pure particulate San Carlos olivine was not an ideal analog for lunar surface compositions. Future studies should use more analogous materials such as lunar simulants or Apollo surface soil samples. Additionally, a procedure would need to be created to minimize the loss of the Apollo soil samples during the sample-making process, which may not be trivial.

Even with more accurate particle size distributions, surface porosities, and compositions, measurements also require a simulated lunar environment to be most comparable to remote and in situ observations of the lunar surface (e.g., Logan and Hunt, 1970; Logan et al., 1973, Donaldson Hanna et al., 2017). Our measurements were made under ambient conditions, which are not representative of the lunar environment (e.g., Logan and Hunt, 1970; Logan et al., 1973). The ambient pressure during our measurements, as compared to the vacuum conditions of the lunar surface resulted in reduced spectral contrast for our measurements and a CF shifted towards lower wavenumbers (e.g., Logan et al., 1973; Donaldson Hanna et al., 2017; Shirley and Glotch, 2019). Future investigations should be made under simulated lunar environmental conditions, such as those achievable by environment chambers at Brown University (Donaldson Hanna et al., 2017), the University of Oxford (Donaldson Hanna et al., 2021), and Stony Brook University (Shirley and Glotch, 2019).

6. CONCLUSIONS

The surface porosity of a particulate material is difficult to quantify; in this study, we estimated the surface porosity of prepared particulate San Carlos olivine samples with the use of an imaging microscope. Through the use of binarization thresholding, we estimated the surface porosity of samples via the analysis of high spatial resolution images (225X magnification) of the sample's surface. In addition, binarization thresholding was a non-destructive technique that gives further usefulness to this methodology.

We investigated how diagnostic spectral features shifted and changed with increased surface porosity and reduced particle size. The position of the TF shifted towards lower wavenumbers for increased surface porosity; however, any shifts observed for reduced particle size appeared to be negligible. This agreed with past studies which suggested only changes in surface porosity shifted the location of the TF. The effects of surface porosity dominate the spectral feature changes due to particle size for the contrasts, areas, and slopes; increased surface porosity effects were between 2.8 and 7.1 times greater than those associated with reduced particle size. For the individual spectral features, we found that the high wavenumber transparency slope increased with increased surface porosity and reduced particle size. The contrast of the CF, the 3rd, 6th, and 9th vibrational bands all displayed reduced contrast with increased surface porosity and reduced particle size. The depth and area of the TF both displayed the opposite effect, increased spectral contrast with increased surface porosity and reduced particle size. The results of this investigation suggest that the spectral effects of increased surface porosity and reduced particle size are difficult to uniquely distinguish from one another, except for the shift in the location of the TF which appears to be uniquely related to the surface porosity.

APPENDIX A:
CUMULATIVE PARTICLE SIZE WEIGHTS

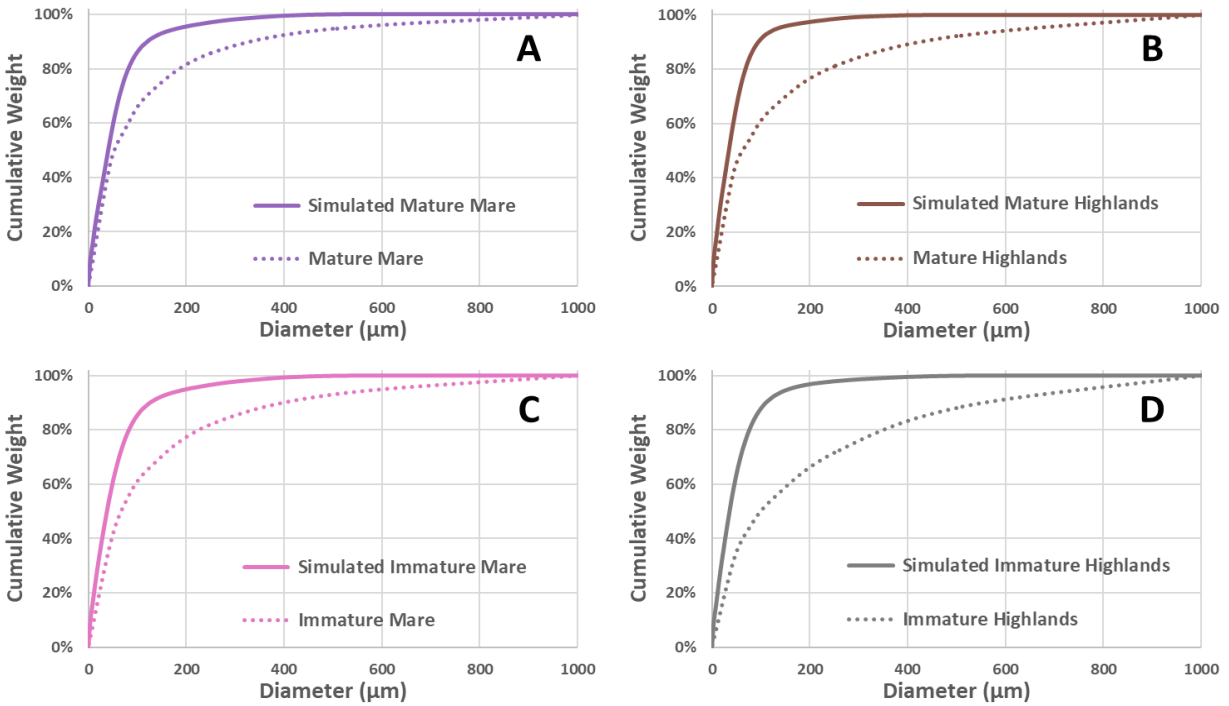


Figure A1: Cumulative weights of the lunar regolith simulants compared to the corresponding lunar particle size distributions tabulated in the Lunar Sample Compendium. Mature mare (A), mature highlands (B), immature mare (C), and immature highlands (D).

In addition to the lack of large particles, our lunar regolith simulants appear to be enriched in smaller diameter material. This again may be due to larger diameter material failing to stay lofted in the solution long enough to be measured by the CILAS particle size analyzer; however, it may be due to how we generated our samples. Our lunar regolith simulants were generated by grinding and sieving and then linearly adding each size fraction; however, all particle diameters are not made linearly, they are made lognormally (Rowan and Becker, 1971). This lognormal distribution was weighted towards smaller particles; therefore, smaller particles should have been generated in a greater abundance than larger particles in each size fraction when grinding material, which skewed the size distribution towards a smaller size fraction when combined to create our lunar regolith simulants (Figure 2).

APPENDIX B:
DEPOSITED SAMPLE SIEVE SIZE DISCUSSION

We chose to use a 75 μm sieve for generating the deposited samples after a brief set of experiments. We passed the $< 45 \mu\text{m}$ sample (the particle size distribution dominated by the finest particle size fraction) and the simulated immature highlands sample (the particle size distribution most heavily weighted towards larger particles) through a 250 μm , 125 μm , 75 μm , and 45 μm sieve in the Divspec apparatus and measured the bulk porosity of the resulting deposited sample. The 250 μm and 125 μm sieved samples each had a similar porosity to that of our leveled samples, due to the larger particles damaging the delicate structures created by the finer particle size fractions. The 75 μm and 45 μm sieved samples were both more porous than the leveled samples. However, the 45 μm sieve only allowed 30% of the original mass fraction of the immature highlands simulant to pass through it. Thus, we selected the 75 μm sieve for this investigation as it resulted in a porosity greater than our other methods, while also preserving 55% (simulated immature highlands) to 68% (simulated mature mare) of the original mass fractions of the simulants. Each simulant was poured into the 75 μm sieve and then shaken by the sieve shaker to deposit material below in and around the sample cup. Material that landed on the sample cup rim was periodically removed during the sample-making process to prevent asymmetric sample formation.

The 75 μm sieve was selected to prevent large particles from damaging our delicately deposited structures; however, fast moving particles could also be a detriment. High velocity particles could be created via interactions with the vibrating sieve. These particles must be slowed down; however, it would take a particle an infinite distance and an infinite time to asymptotically reach its terminal velocity. This distance can be approximated using Equation A1 which can be derived via Stokes (1850). The height (ℓ) a spherical particle would fall before it encountered its mass in atmosphere is given by:

$$\ell = \frac{2D}{3} \frac{\rho_{crystal}}{\rho_{air}} \quad (A1)$$

where D is the effective diameter (the diameter the particle would have if it was a sphere) of the particle, $\rho_{crystal}$ is the crystal density of the particle, taken as 3.355 g/cm^3 (Abrahamson et al., 1997), and ρ_{air} is the density of air at standard temperature and pressure. Using Equation 1, as an example, a $75 \text{ }\mu\text{m}$ diameter particle of olivine that falls directly downwards, through an atmospheric density of $1.225 \times 10^{-3} \text{ g/cm}^3$, would encounter its mass in atmosphere after it fell roughly 13.5 cm . Our height of 46 cm should prevent particles that had achieved higher velocities sufficient time to be reduced in velocity before coming into contact with the sample cup.

APPENDIX C:
HIGH WAVENUMBER TRANSPARENCY SLOPE VS. DEPTH OF THE
3RD VIBRATION BAND

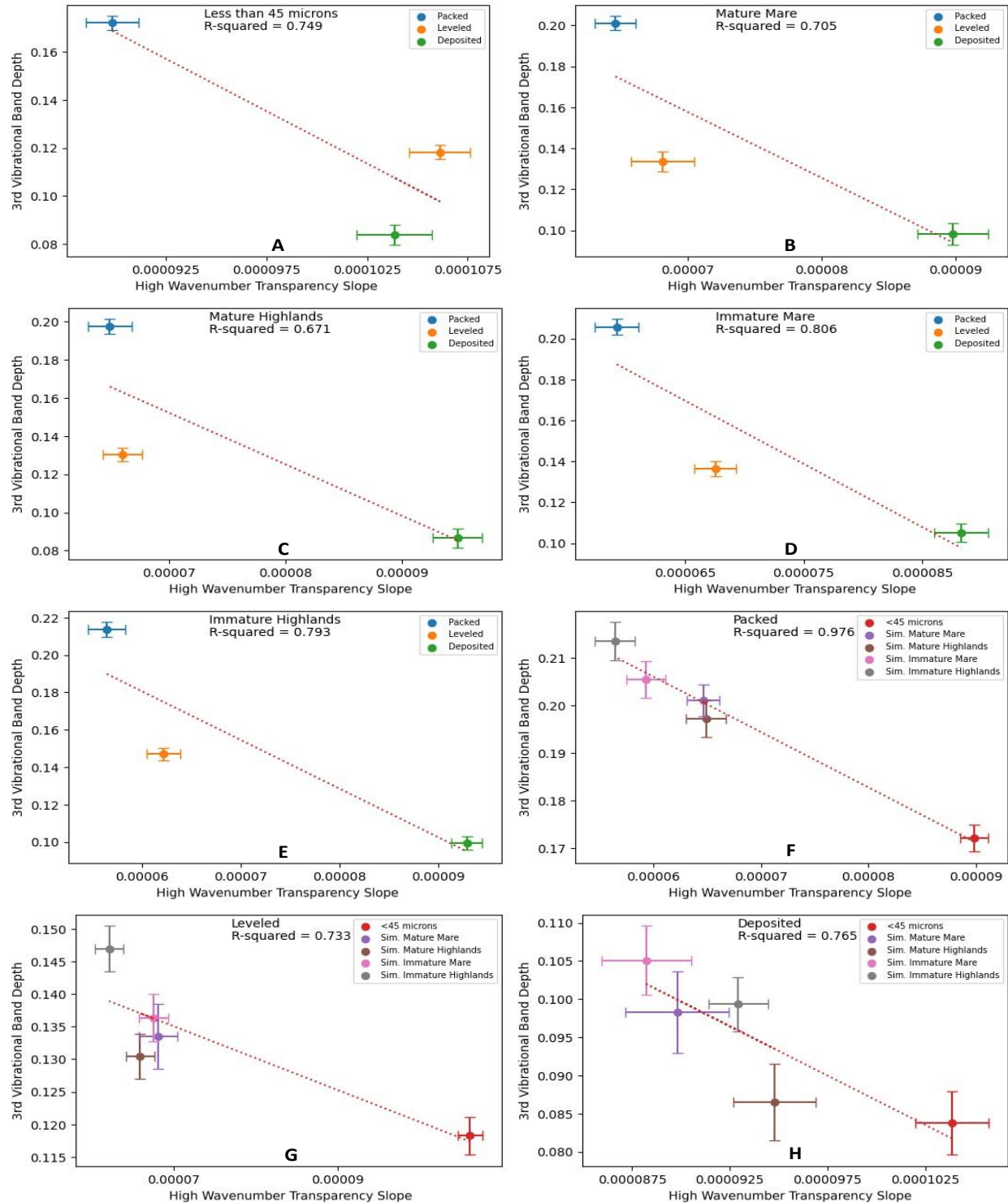


Figure A2: All five of the constant particle size (A-E) trendline plots and all three of the constant porosity (F-H) trendline plots for the High Wavenumber Transparency Slope vs. the depth of the 3rd vibration band. (A) < 45 μm , (B) simulated mature mare, (C) simulated mature highlands, (D) simulated immature mare, and (E) simulated immature highlands.

APPENDIX D:
HIGH WAVENUMBER TRANSPARENCY SLOPE VS. CF SPECTRAL
DEPTH

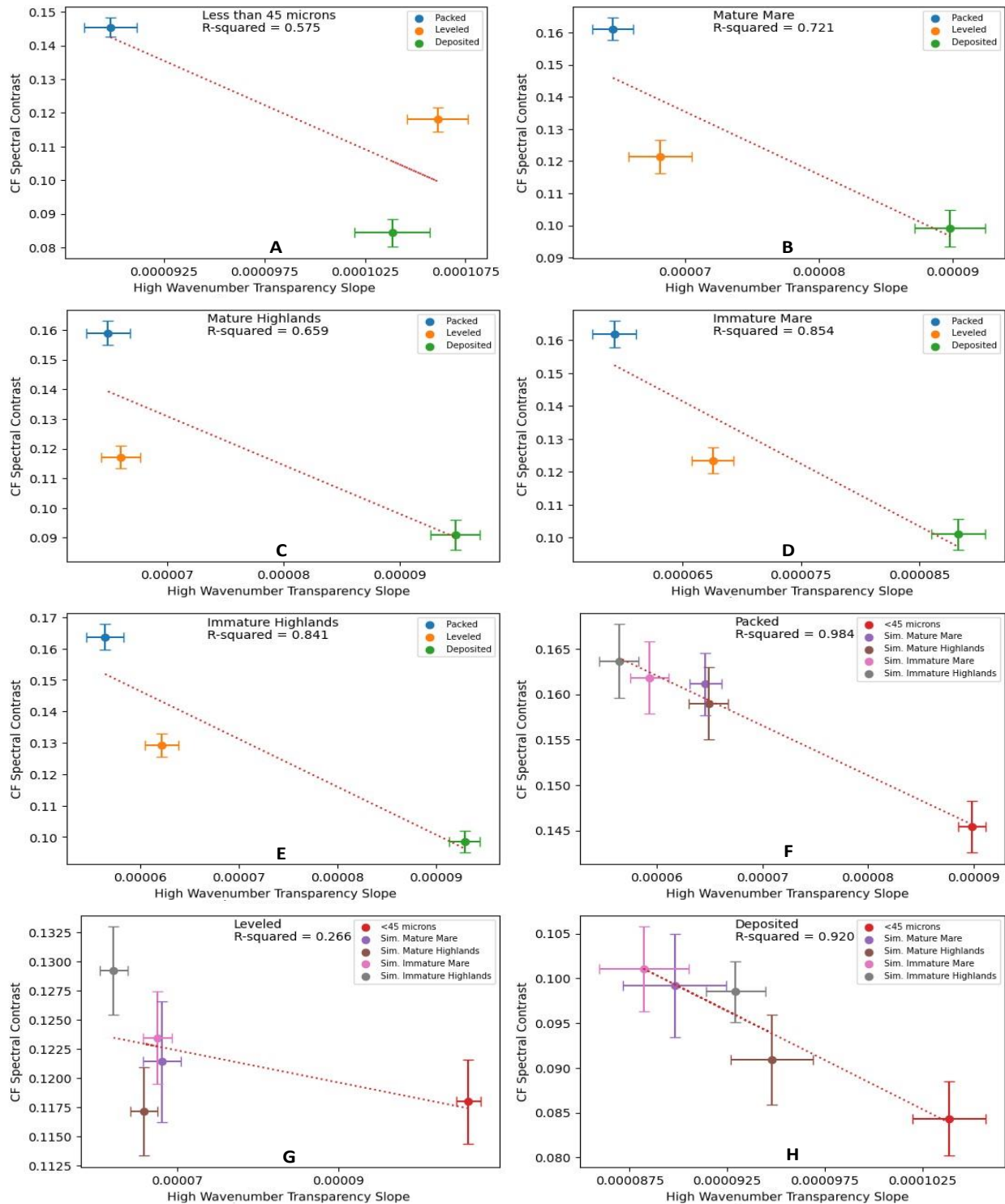


Figure A3: All five of the constant particle size (A-E) trendline plots and all three of the constant porosity (F-H) trendline plots for the High Wavenumber Transparency Slope vs. the spectral contrast of the CF. (A) < 45 μm , (B) simulated mature mare, (C) simulated mature highlands, (D) simulated immature mare, and (E) simulated immature highlands.

APPENDIX E:
HIGH WAVENUMBER TRANSPARENCY SLOPE VS. TF AREA

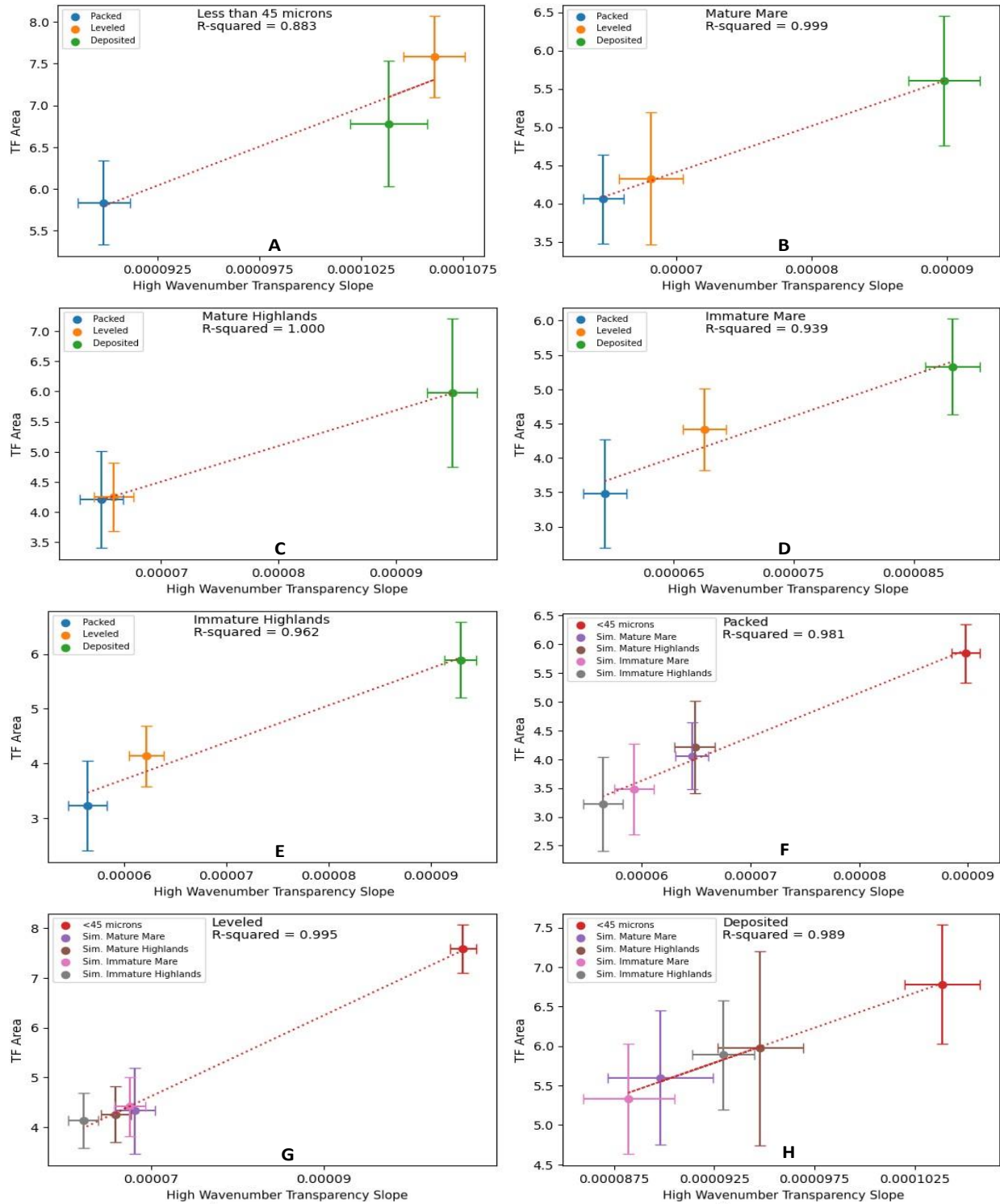


Figure A4: All five of the constant particle size (A-E) trendline plots and all three of the constant porosity (F-H) trendline plots for the High Wavenumber Transparency Slope vs. the area of the TF. (A) < 45 μm , (B) simulated mature mare, (C) simulated mature highlands, (D) simulated immature mare, and (E) simulated immature highlands.

APPENDIX F:
HIGH WAVENUMBER TRANSPARENCY SLOPE VS. TF DEPTH

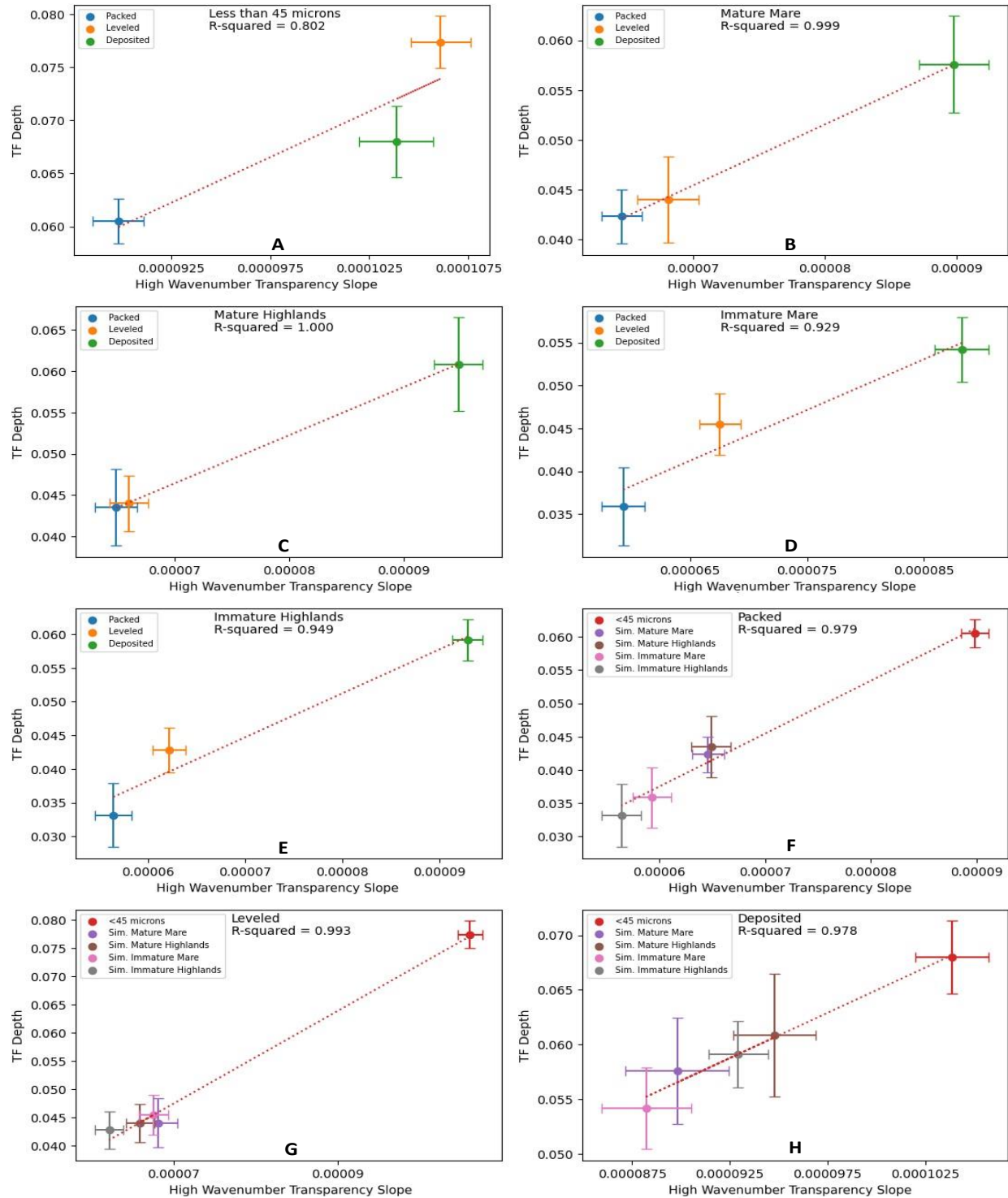


Figure A5: All five of the constant particle size (A-E) trendline plots and all three of the constant porosity (F-H) trendline plots for the High Wavenumber Transparency Slope vs. the depth of the TF. (A) < 45 μm , (B) simulated mature mare, (C) simulated mature highlands, (D) simulated immature mare, and (E) simulated immature highlands.

APPENDIX G:
DEPTH OF THE 3RD VIBRATION BAND VS. CF SPECTRAL DEPTH

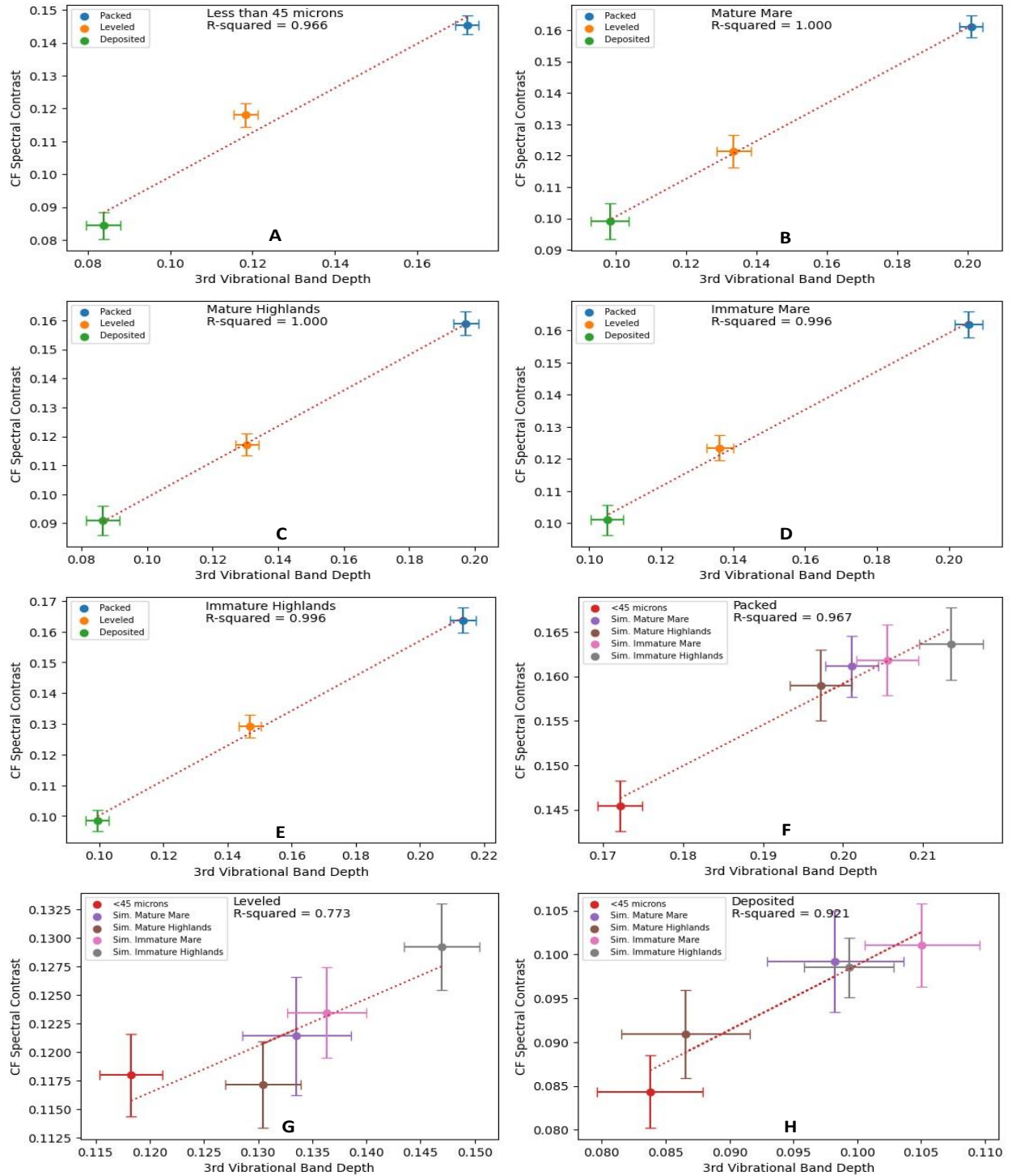


Figure A6: All five of the constant particle size (A-E) trendline plots and all three of the constant porosity (F-H) trendline plots for the depth of the 3rd vibration band vs. the spectral contrast of the CF. (A) < 45 μm , (B) simulated mature mare, (C) simulated mature highlands, (D) simulated immature mare, and (E) simulated immature highlands.

APPENDIX H:
DEPTH OF THE 3RD VIBRATION BAND VS. TF AREA

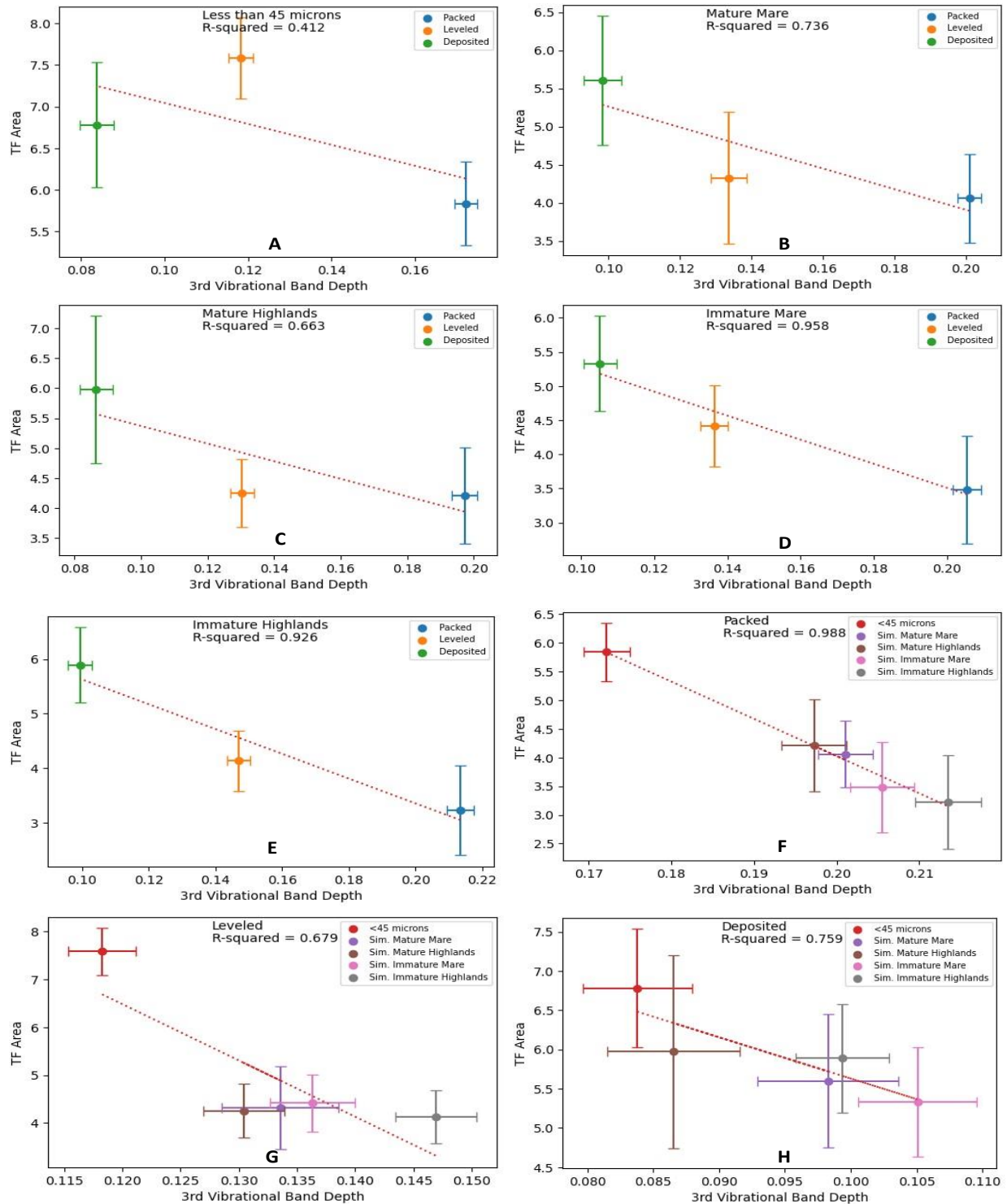


Figure A7: All five of the constant particle size (A-E) trendline plots and all three of the constant porosity (F-H) trendline plots for the depth of the 3rd vibration band vs. the area of the TF. (A) < 45 μm , (B) simulated mature mare, (C) simulated mature highlands, (D) simulated immature mare, and (E) simulated immature highlands.

APPENDIX I:
DEPTH OF THE 3RD VIBRATION BAND VS. TF DEPTH

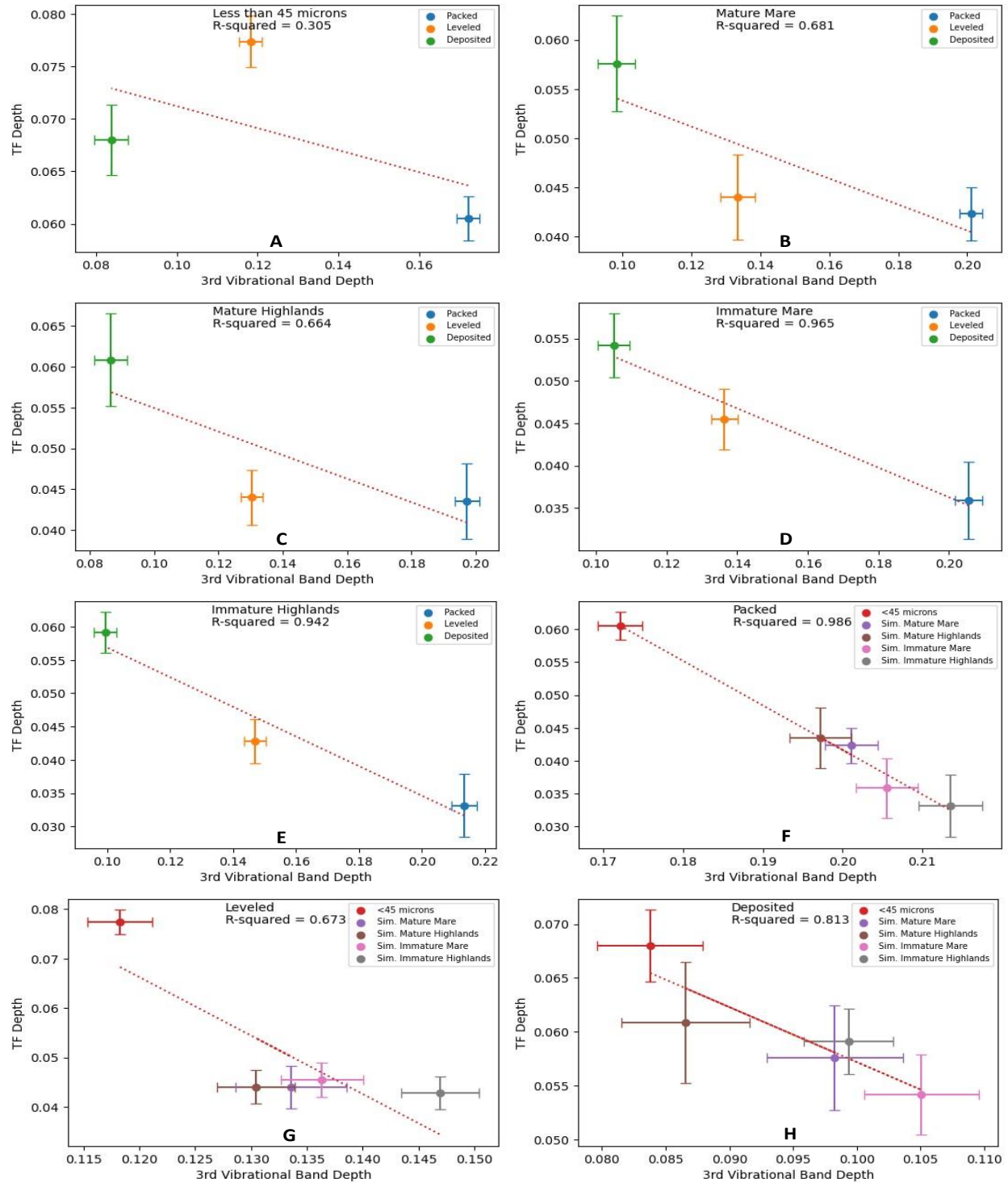


Figure A8: All five of the constant particle size (A-E) trendline plots and all three of the constant porosity (F-H) trendline plots for the depth of the 3rd vibration band vs. the depth of the TF. (A) < 45 μm , (B) simulated mature mare, (C) simulated mature highlands, (D) simulated immature mare, and (E) simulated immature highlands.

APPENDIX J:
CF SPECTRAL DEPTH VS. TF AREA

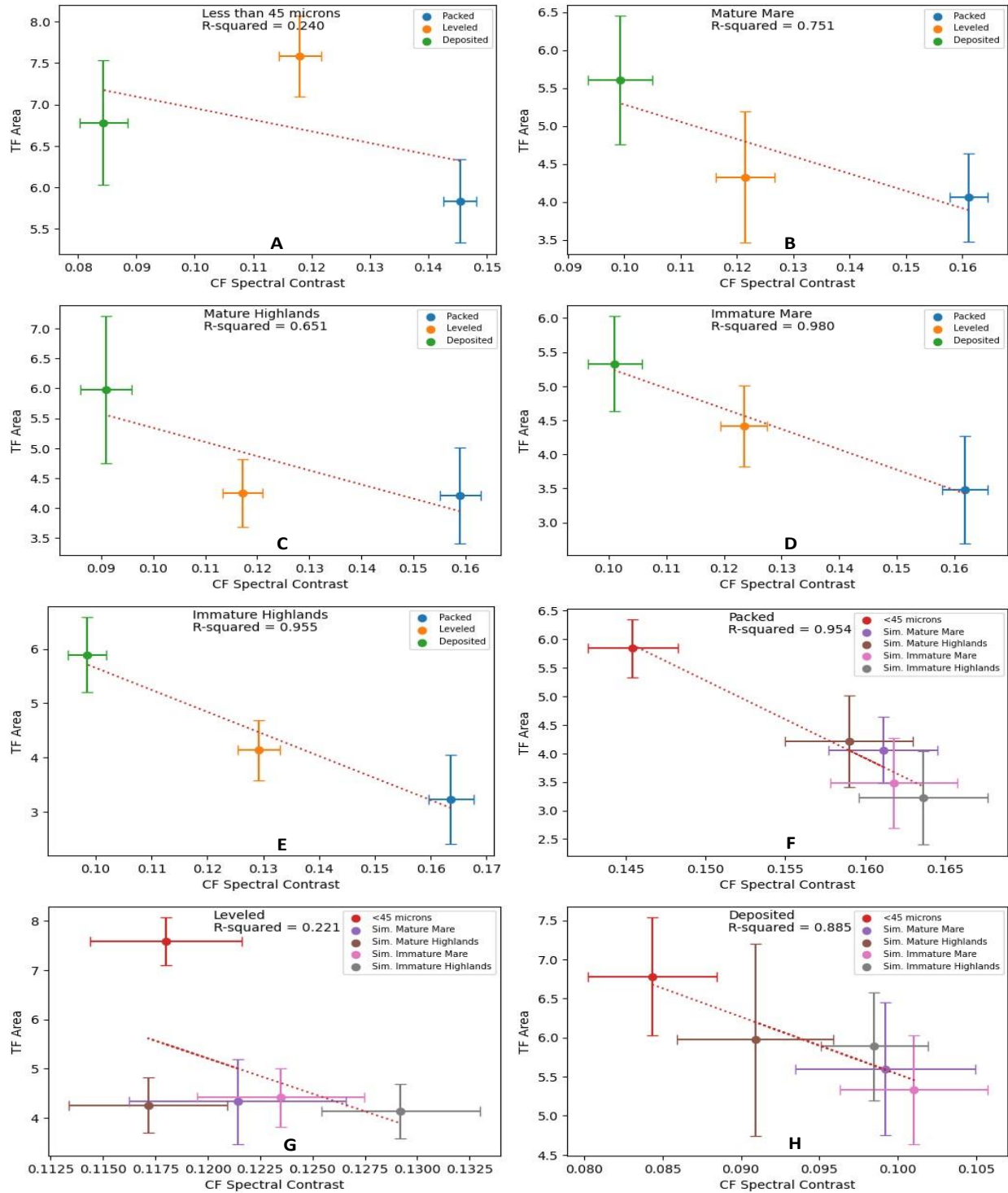


Figure A9: All five of the constant particle size (A-E) trendline plots and all three of the constant porosity (F-H) trendline plots for the spectral contrast of the CF vs. the area of the TF. (A) < 45 μm , (B) simulated mature mare, (C) simulated mature highlands, (D) simulated immature mare, and (E) simulated immature highlands.

APPENDIX K:
CF SPECTRAL DEPTH VS. TF DEPTH

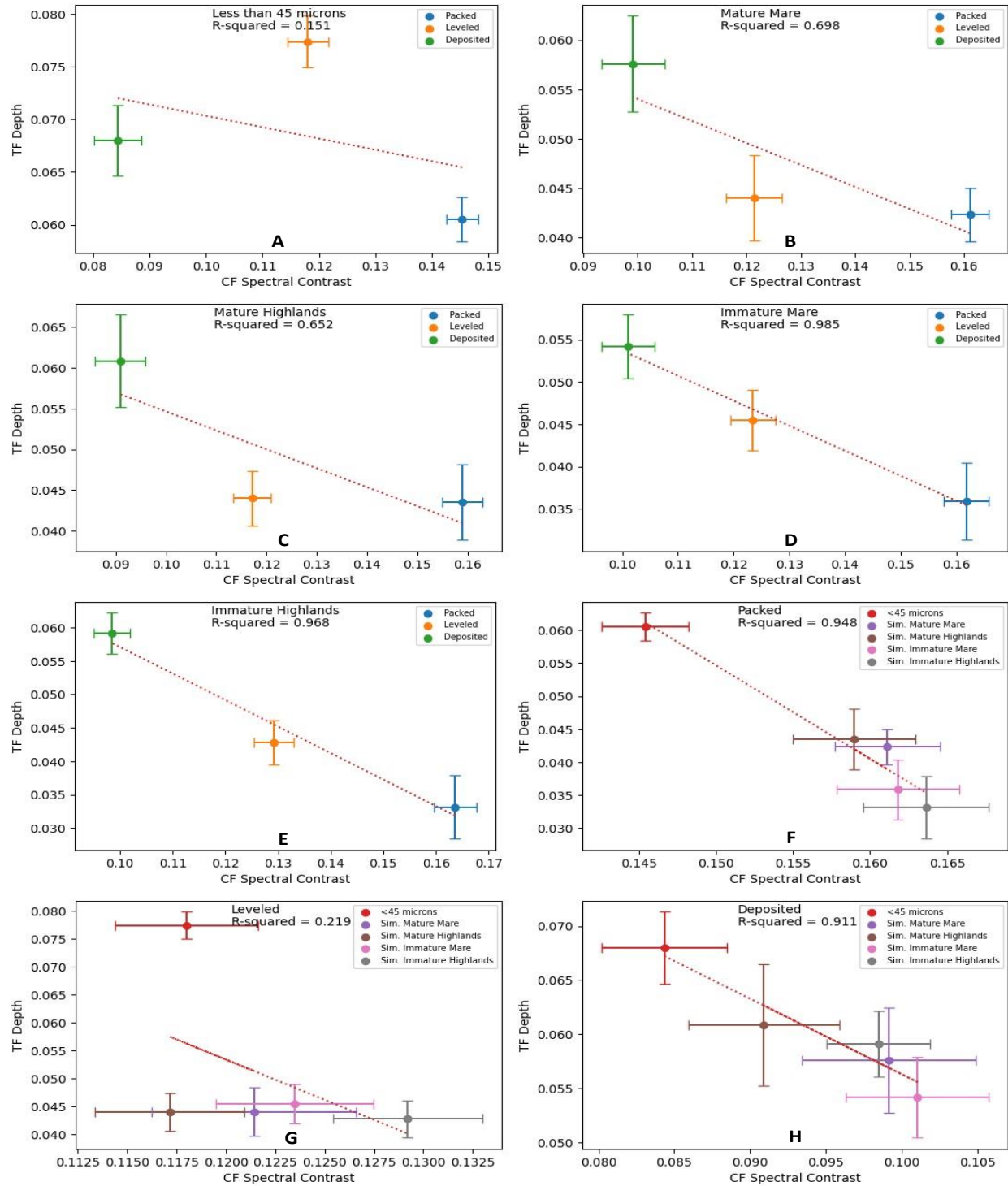


Figure A10: All five of the constant particle size (A-E) trendline plots and all three of the constant porosity (F-H) trendline plots for the spectral contrast of the CF vs. the depth of the TF. (A) < 45 μm , (B) simulated mature mare, (C) simulated mature highlands, (D) simulated immature mare, and (E) simulated immature highlands.

**APPENDIX L:
TF AREA VS. TF DEPTH**

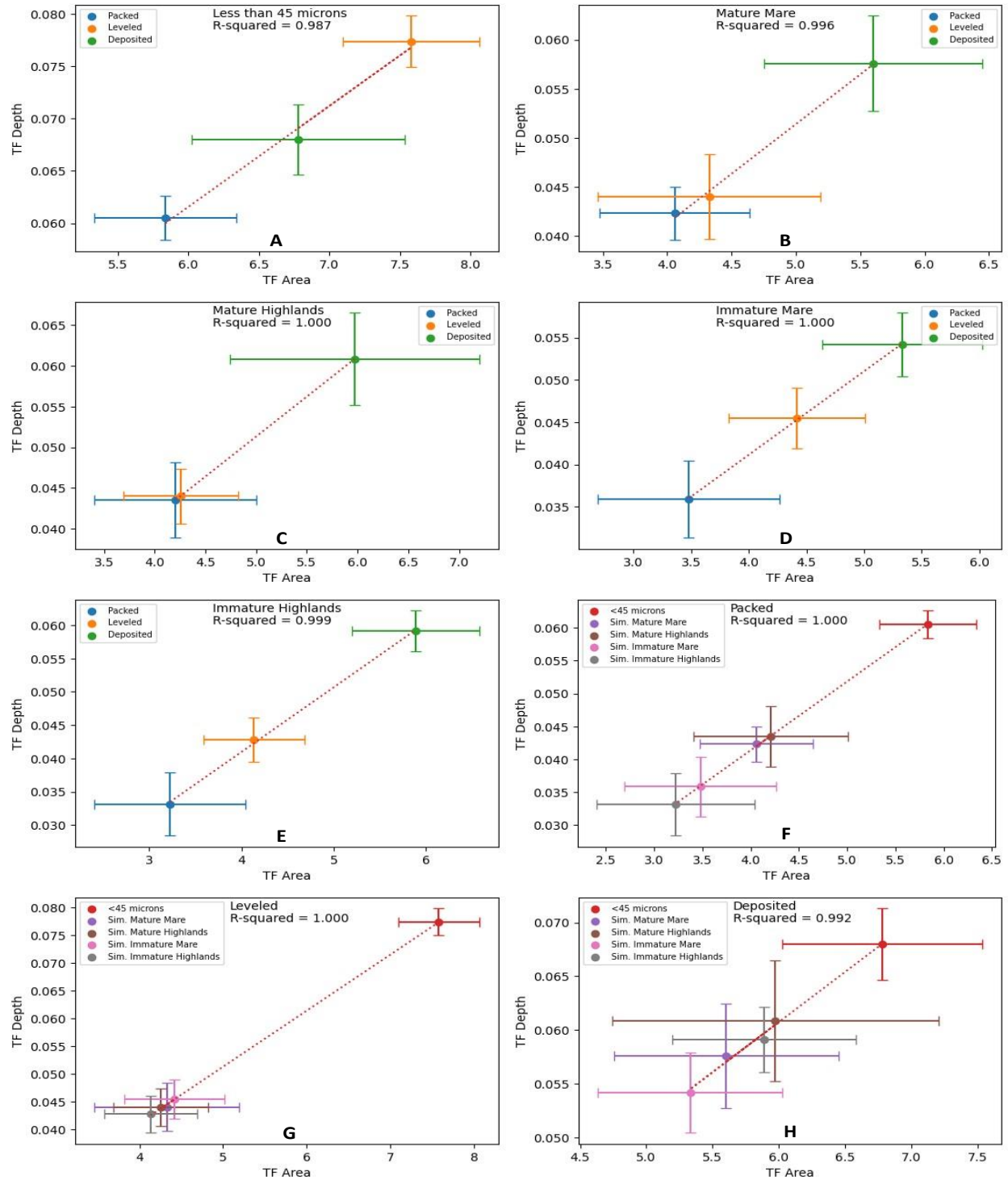


Figure A11: All five of the constant particle size (A-E) trendline plots and all three of the constant porosity (F-H) trendline plots for the area of the TF vs. the depth of the TF. (A) $< 45 \mu\text{m}$, (B) simulated mature mare, (C) simulated mature highlands, (D) simulated immature mare, and (E) simulated immature highlands.

APPENDIX M:
COMBINED TRENDLINE PLOTS - HIGH WAVENUMBER
TRANSPARENCY SLOPE

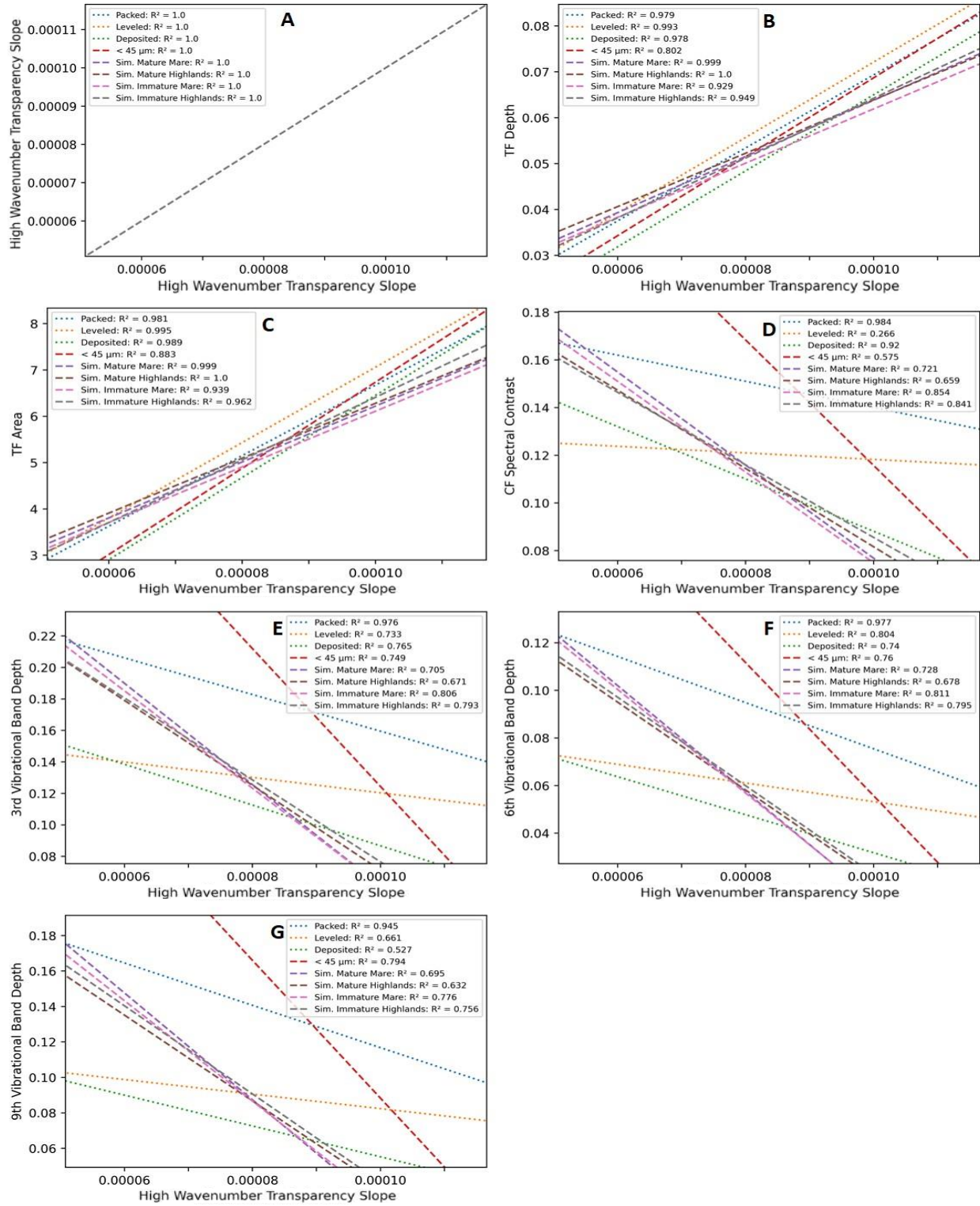


Figure A12: Combined trendline plots for the High Wavenumber Transparency Slope vs. the High Wavenumber Transparency Slope (A), the TF depth (B), the TF area (C), the CF spectral contrast (D), the 3rd vibrational band (E), the 6th vibrational band (F), and the 9th vibrational band (G).

APPENDIX N:
COMBINED TRENDLINE PLOTS - TF AREA

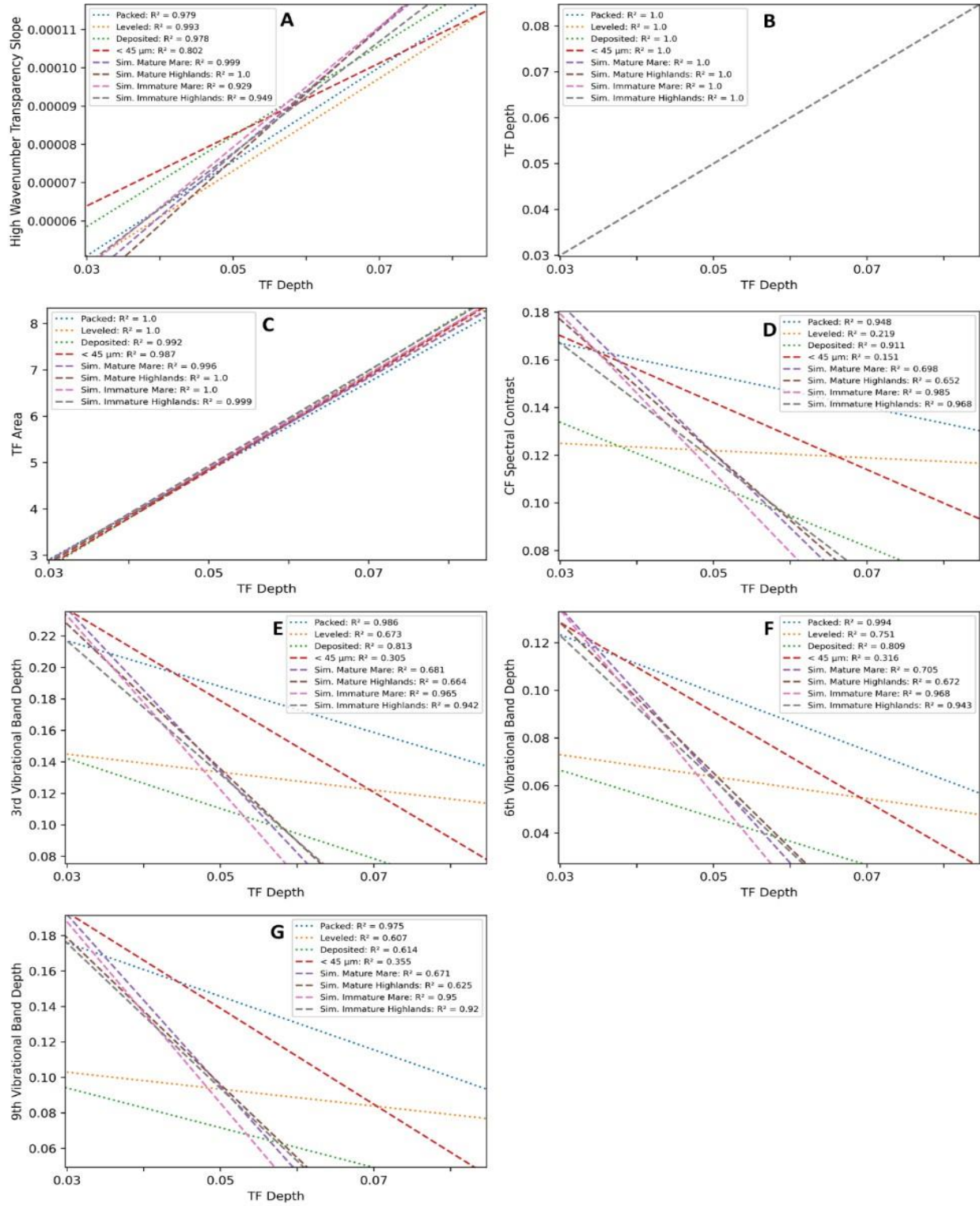


Figure A13: Combined trendline plots for the TF depth vs. the High Wavenumber Transparency Slope (A), the TF depth (B), the TF area (C), the CF spectral contrast (D), the 3rd vibrational band (E), the 6th vibrational band (F), and the 9th vibrational band (G).

**APPENDIX O:
COMBINED TRENDLINE PLOTS - TF DEPTH**

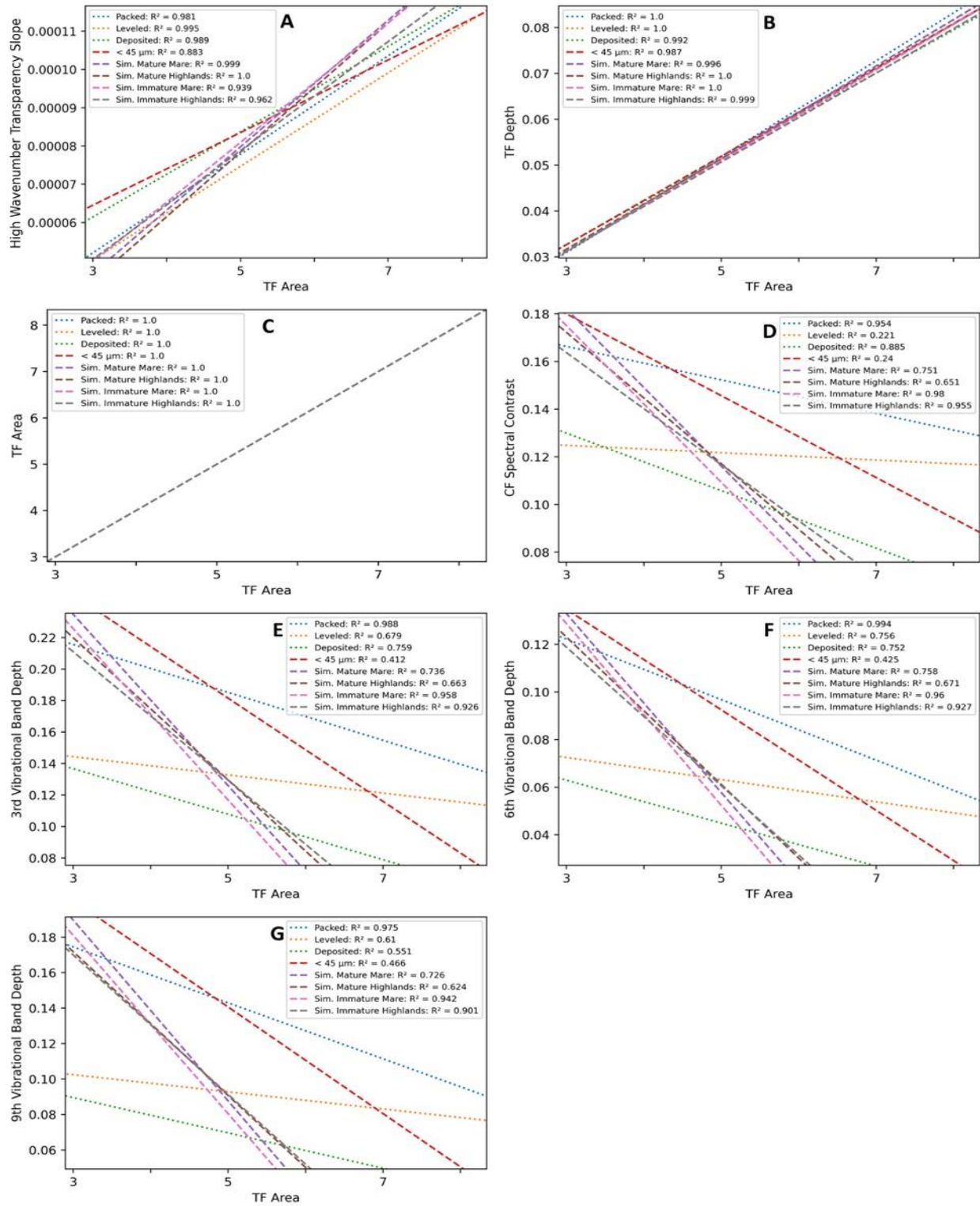


Figure A14: Combined trendline plots for the TF area vs. the High Wavenumber Transparency Slope (A), the TF depth (B), the TF area (C), the CF spectral contrast (D), the 3rd vibrational band (E), the 6th vibrational band (F), and the 9th vibrational band (G).

APPENDIX P:
COMBINED TRENDLINE PLOTS - CF SPECTRAL DEPTH

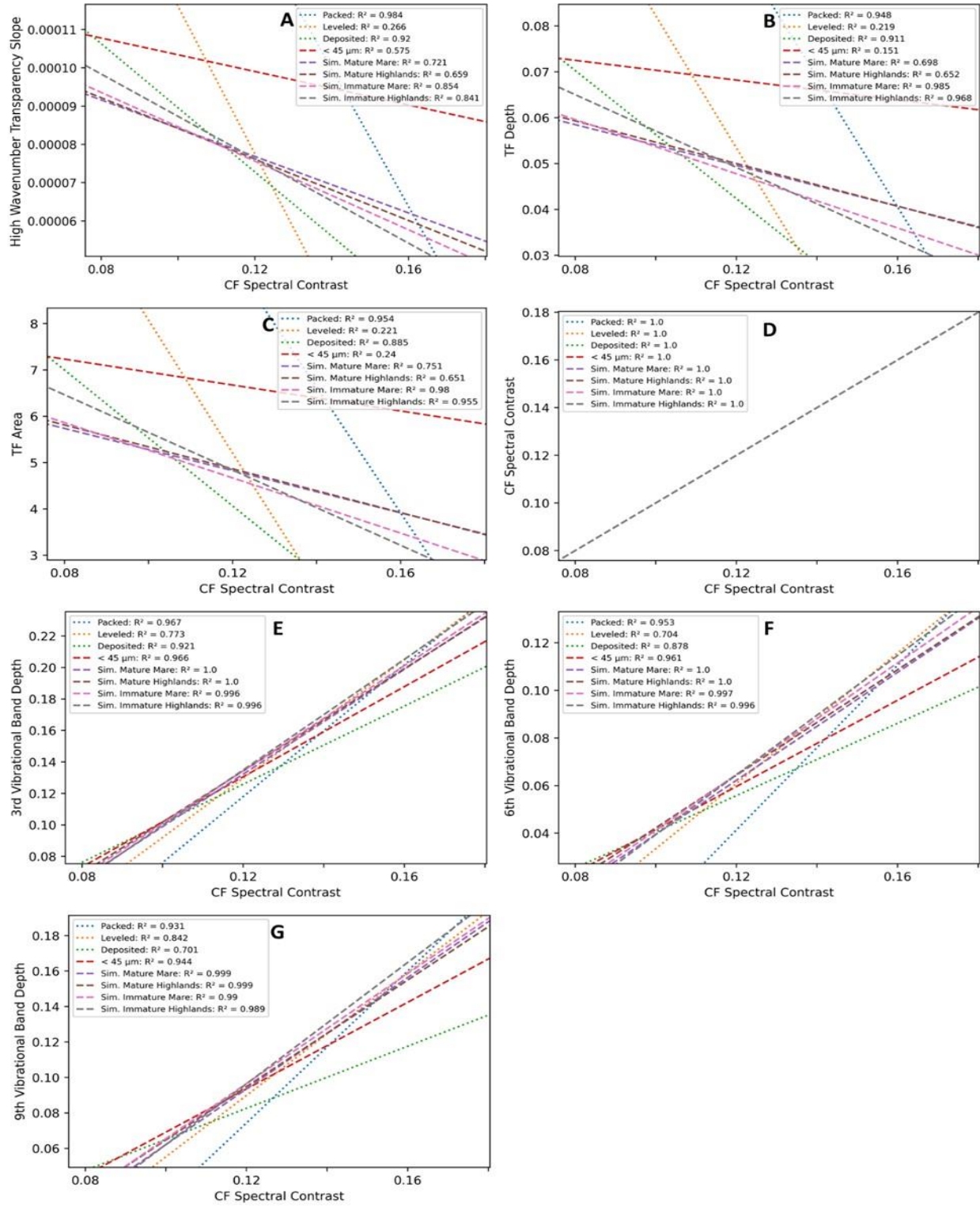


Figure A15: Combined trendline plots for the CF spectral contrast vs. the High Wavenumber Transparency Slope (A), the TF depth (B), the TF area (C), the CF spectral contrast (D), the 3rd vibrational band (E), the 6th vibrational band (F), and the 9th vibrational band (G).

APPENDIX Q:
COMBINED TRENDLINE PLOTS - DEPTH OF THE 3RD VIBRATION
BAND

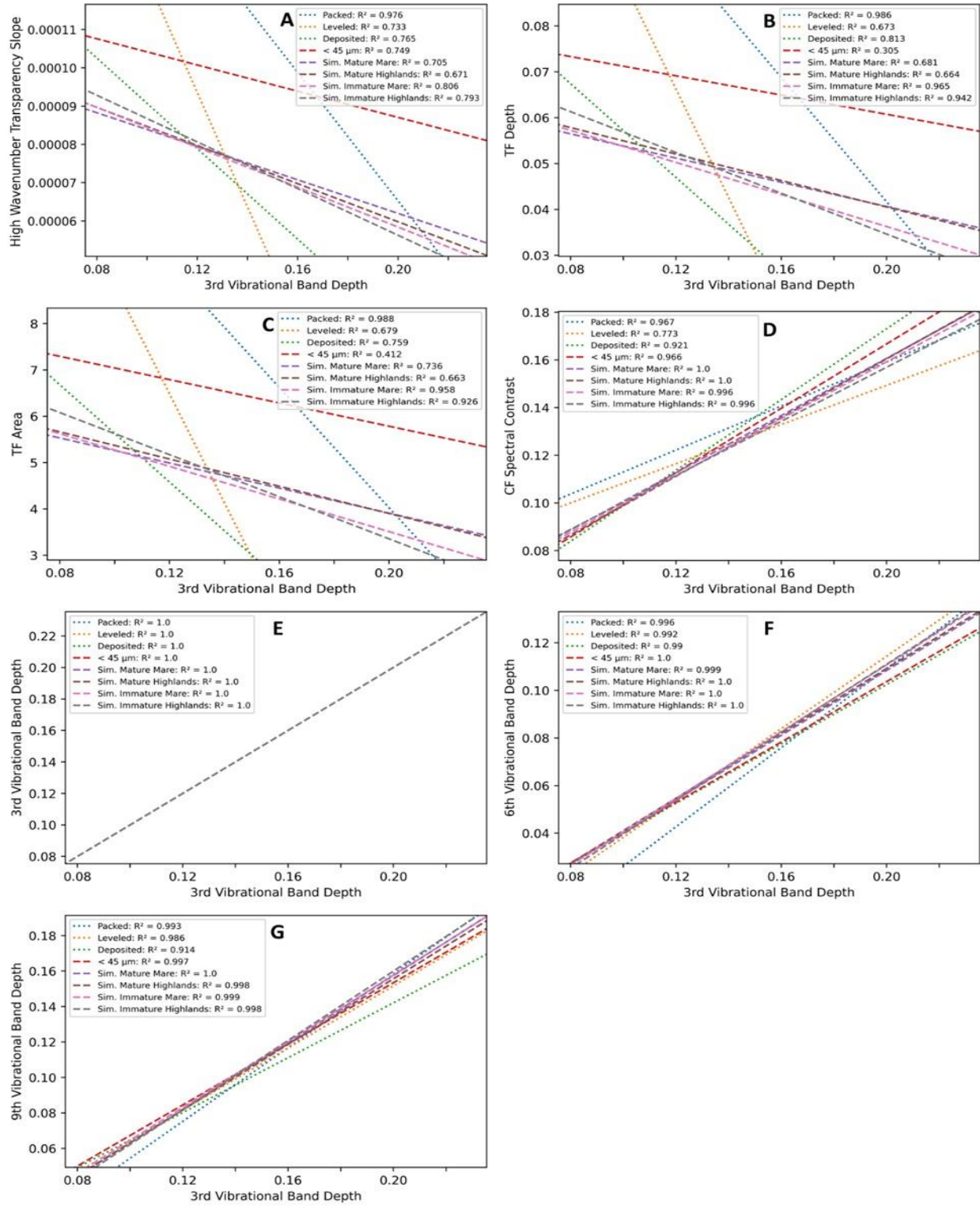


Figure A16: Combined trendline plots for the 3rd vibrational band vs. the High Wavenumber Transparency Slope (A), the TF depth (B), the TF area (C), the CF spectral contrast (D), the 3rd vibrational band (E), the 6th vibrational band (F), and the 9th vibrational band (G).

APPENDIX R:
COMBINED TRENDLINE PLOTS - DEPTH OF THE 6TH VIBRATION
BAND

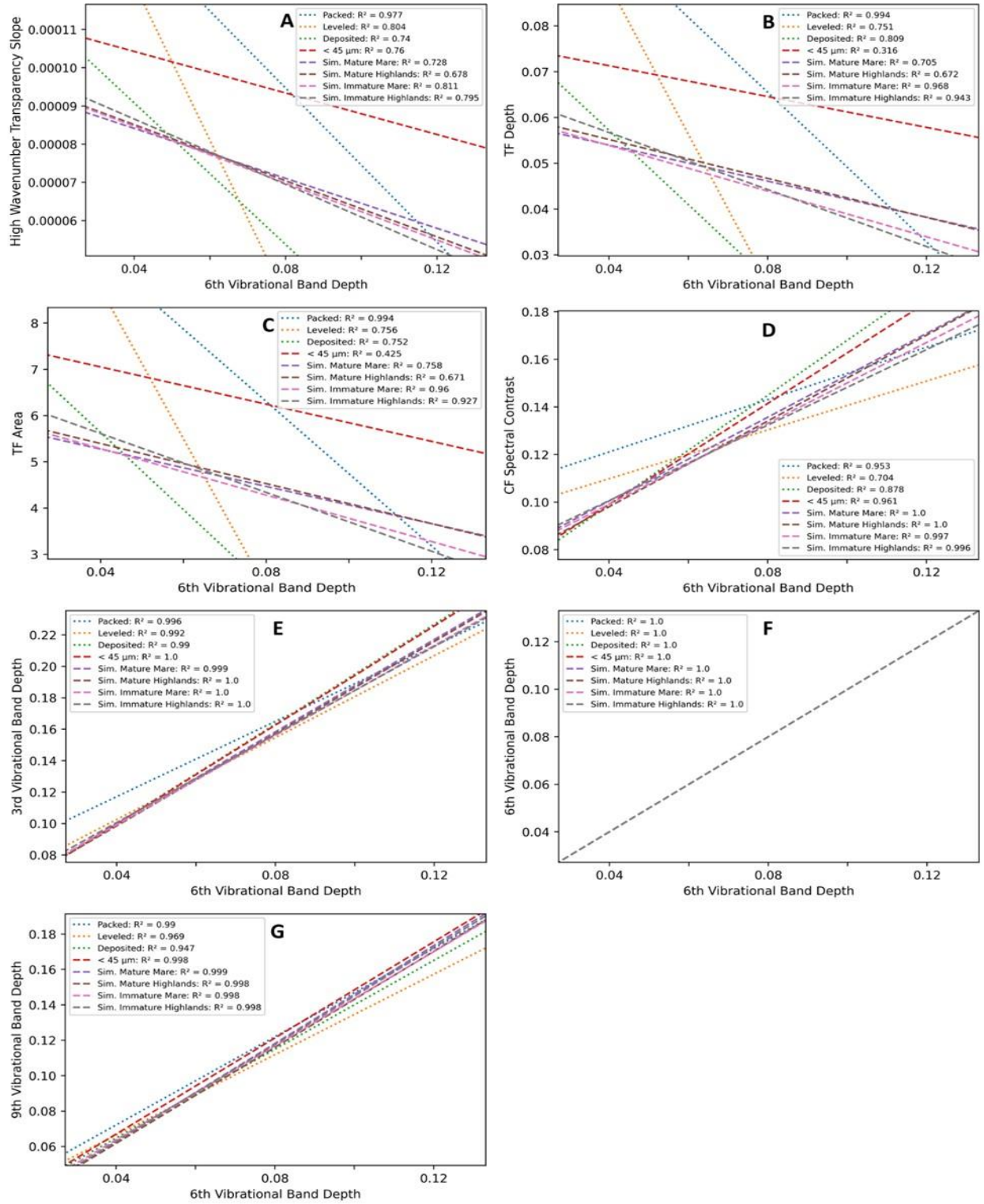


Figure A17: Combined trendline plots for the 6th vibrational band vs. the High Wavenumber Transparency Slope (A), the TF depth (B), the TF area (C), the CF spectral contrast (D), the 3rd vibrational band (E), the 6th vibrational band (F), and the 9th vibrational band (G).

APPENDIX S:
COMBINED TRENDLINE PLOTS - DEPTH OF THE 9TH VIBRATION
BAND

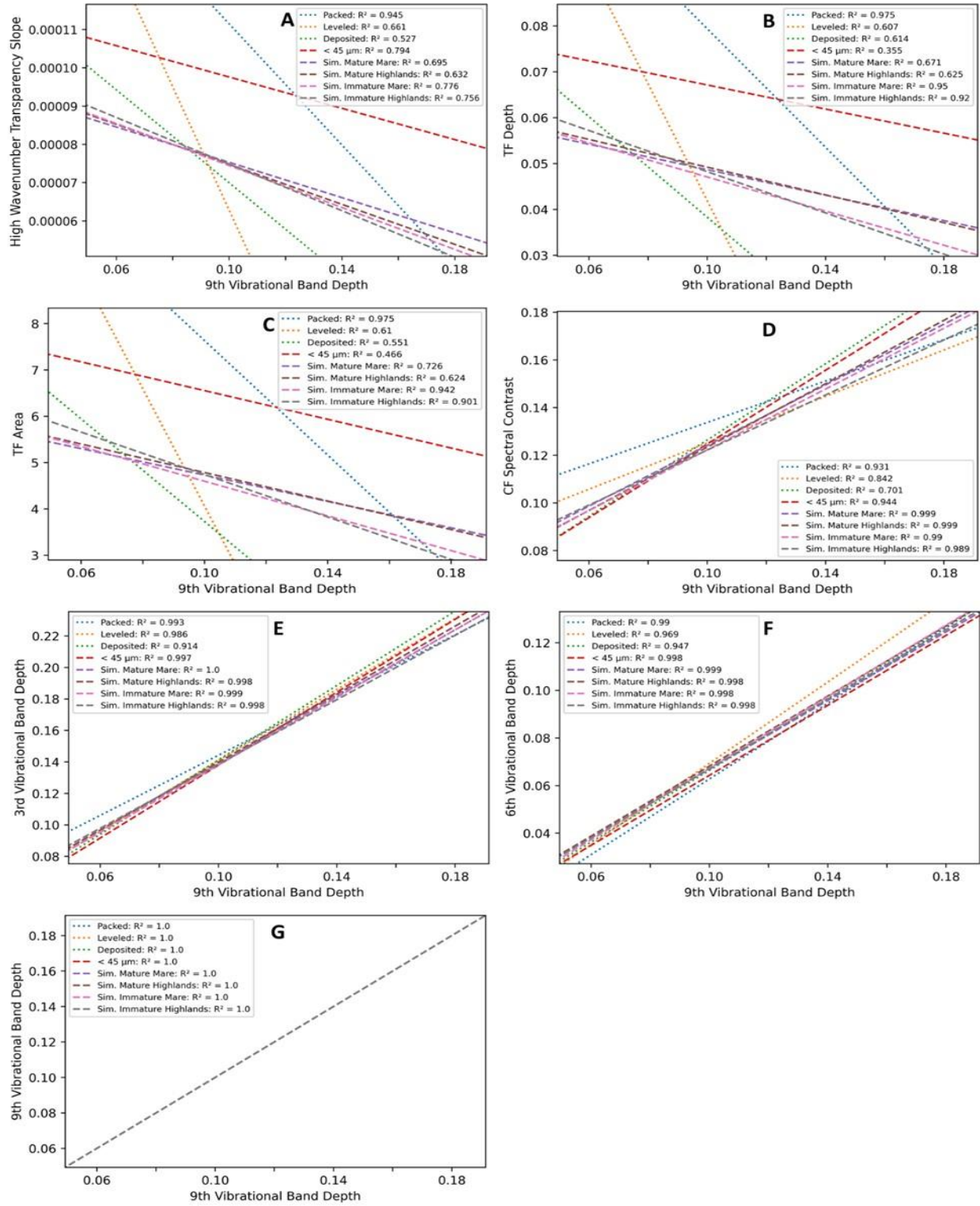


Figure A18: Combined trendline plots for the 9th vibrational band vs. the High Wavenumber Transparency Slope (A), the TF depth (B), the TF area (C), the CF spectral contrast (D), the 3rd vibrational band (E), the 6th vibrational band (F), and the 9th vibrational band (G).

LIST OF REFERENCES

- Abramson, E. H., Brown, J. M., Slutsky, L. J., and Zaug, J. (1997). The elastic constants of San Carlos olivine to 17 GPa. *Journal of Geophysical Research: Solid Earth*, 102(B6), 12253–12263. doi:10.1029/97jb00682.
- Arnold, J. A., Schräpler, R., Donaldson Hanna, K.L., Lindsay, S.S., Bowles, N.E., Blum, J. (2016). The Effect of Porosity on Infrared Spectra. 47th Lunar and Planetary Science Conference, The Woodlands, TX.
- Bates, H. C., King, A. J., Donaldson Hanna, K. L., Bowles, N. E., and Russell, S. S. (2019). Linking mineralogy and spectroscopy of highly aqueously altered CM and CI carbonaceous chondrites in preparation for primitive asteroid sample return. *Meteoritics and Planetary Science*. doi:10.1111/maps.13411.
- Blum, J., Schrapler, R., Davidsson, B. J. R., and Trigo-Rodriguez, J. M. (2006). The Physics of Protoplanetesimal Dust Agglomerates. I. Mechanical Properties and Relations to Primitive Bodies in the Solar System. *The Astrophysical Journal*, 652(2), 1768–1781. doi:10.1086/508017.
- Burns, R.G., Huggins, F.E. (1972). Cation determinative curves for Mg–Fe–Mn olivines from vibrational spectra. *Am. Miner.* 57, 967–985.
- Butler, J.C., and King, E.A. (1974) Analysis of the grain size-frequency distributions of lunar fines. *Proc. 5th Lunar Sci. Conf.* 829-841.
- Carrier W.D. et al. (1991) In *Lunar Sourcebook* (Heiken G.H., Vaniman D.T., and French B.M., Eds.), pp. 475–594. Cambridge University Press.

- Clark, R., Swayze, G., Wise, R., Livo, E., Hoefen, T., Kokaly, R., and Sutley, S. (2007). USGS digital spectral library splib06a. U.S. Geological Survey Denver, CO, rev. sept. 20, 2007. edition. Digital Data Series 231.
- Cooper, B. L., Salisbury, J. W., Killin, R. M., Potter, A. E. (2002). Midinfrared spectral features of rocks and their powders. *Journal of Geophysical Research*, 107(E4). doi:10.1029/2000je001462.
- Conel, J. E. (1969). Infrared emissivities of silicates: Experimental results and a cloudy atmosphere model of spectral emission from condensed particulate mediums, *Journal of Geophysical Research*, 74, 1614 – 1634.
- Donaldson Hanna, K. L., Greenhagen, B. T., Patterson III, W. R., Pieters, C. M., Mustard, J. F., Bowles, N. E., Paige, D. A., Glotch, T. D., and Thompson, C. (2017). Effects of varying environmental conditions on emissivity spectra of bulk lunar soils: Application to Diviner thermal infrared observations of the Moon. *Icarus*, 283, 326-342.
- Donaldson Hanna, K. L., Schrader, D.L., Cloutis, E.A., Cody, G.D., King, A.J., McCoy, T.J., Applin, D.M., Mann, J.P., Bowles, N.E., Brucato, J.R., Connolly Jr., H.C., Dotto, E., Keller, L.P., Lim, L.F., Clark, B.E., Hamilton, V.E., Lantz, C., Lauretta, D.S., Russell, S.S., and Schofield, P.F. (2019). Spectral characterization of analog samples in anticipation of OSIRIS-REx's arrival at Bennu: A blind test study. *Icarus*, 319, 701–723. doi:10.1016/j.icarus.2018.10.018.
- Donaldson Hanna, K. L., Bowles, N. E., Warren, T. J., Hamilton, V. E., Schrader, D. L., McCoy, T. J., et al. (2021). Spectral characterization of Bennu analogs using PASCAL: A new

- experimental set-up for simulating the near-surface conditions of airless bodies. *Journal of Geophysical Research: Planets*, 126, e2020JE006624. <https://doi.org/10.1029/2020JE006624>.
- Estep-Barnes, P. A. (1977). *Infrared Spectroscopy*. Ch. 11, *Physical Methods in Determinative Mineralogy*.
- Feynman, L. S. (1963). *Lectures on Physics*, Vol. I. Ch. 32, p. 32-1 – 32-8, Addison-Wesley, Reading, MA.
- Graf J.C. (1993). *Lunar Soils Grain Size Catalog*. NASA Pub. 1265.
- Hapke, B. (1993). *Theory of Reflectance and Emittance Spectroscopy*, p. 224. Cambridge University Press.
- Hapke, B., Van Horn, H. (1963). Photometric studies of complex surfaces with applications to the Moon. *Journal of Geophysical Research*, 68, 4545–4570. doi:10.1029/JZ068i015p04545.
- Hamilton, V.E. (2010). Thermal infrared (vibrational) spectroscopy of Mg–Fe olivines: A review and applications to determining the composition of planetary surfaces. *Chemie Der Erde - Geochemistry*, 70, 7-33.
- Henderson, B.G., Jakosky, B.M. (1994). Near-surface thermal gradients and their effects on mid-infrared emission spectra of planetary surfaces. *Journal of Geophysical Research*, 99 (E9), 19,063–19,073.
- Henderson, B.G., Jakosky, B.M. (1997). Near-surface thermal gradients and mid-IR emission spectra: A new model including scattering and application to real data. *Journal of Geophysical Research*, 102, 6567–6580.

- Hovis, W. A., and W. R. Callahan (1966). Infrared reflectance spectra of igneous rocks, tufts, and red sandstone from 0.5 to 22 μm . *J. Opt. Soc. Amer.* 56, 639-643.
- Hunt, G. R., and Salisbury, J. W. (1969). Mid-infrared spectroscopic observations of the Moon. *Philos. Trans. R. Soc. London, Ser. A*, 264, 109 – 139.
- King, E.A., Butler, J.C., and Carman, M.F. (1971). The lunar regolith as sampled by Apollo 11 and 12: Grain size analyses, modal analyses, and origins of particles. *Proc. 2nd Lunar Sci. Conf.* 737-746.
- King, E.A., Butler, J.C., and Carman, M.F. (1972). Chondrules in Apollo 14 samples and size analyses of Apollo 14 and 15 fines. *Proc. 3rd Lunar Sci. Conf.* 673-686.
- Kokaly, R.F., Clark, R.N., Swayze, G.A., Livo, K.E., Hoefen, T.M., Pearson, N.C., Wise, R.A., Benz, W.M., Lowers, H.A., Driscoll, R.L., and Klein, A.J. (2017). USGS Spectral Library Version 7: U.S. Geological Survey Data Series 1035, 61 p., <https://doi.org/10.3133/ds1035>.
- Lyon, R. J. P. (1964). Evaluation of infrared spectrophotometry for compositional analysis of lunar and planetary soils, 2, Rough and powdered surfaces, NASA Rept. CR-100.
- Meyer, C. (2009). Lunar Sample Compendium. Technical Report, 06.
- Morris R. V. (1976). Surface exposure indices of lunar soils: A comparative FMR study. *Proc. Lunar Sci. Conf.* 7th, 315-335.
- Ohtake, M., et al. (2010). Deriving the absolute reflectance of lunar surface using SELENE (Kaguya) multiband imager data. *Space Sci. Rev.* 154, 57–77.

- Pieters, C. M., Fischer, E. M., Rode, O., and Basu, A. (1993). Optical effects of space weathering: The role of the finest fraction. *Journal of Geophysical Research*, 98, 20,817–20,824. <https://doi.org/10.1029/93JE02467>
- Potter, A. E., and Morgan, T. H. (1981). Observations of silicate reststrahlen bands in lunar infrared spectra, *Proc. Lunar Planet Sci. Conf.*, 12B, 703 – 713.
- Rowan, R. J., and Becker, G. W. (1971). Batch Grinding Model. New Mexico Bureau of Mines and Mineral Resources Circular 117. New Mexico.
- Rubens, H., and Nichols, E. F. (1897). Certain Optical and Electro-Magnetic Properties of Heat Waves of Great Wave-Length, I. *Physical Review (Series I)*, 5(2), 98–112. doi:10.1103/physrevseriesi.5.98.
- Ruff, S. W., Christensen, P. R., Barbera, P. W., and Anderson, D. L. (1997). Quantitative thermal emission spectroscopy of minerals: a laboratory technique for measurement and calibration. *Journal of Geophysical Research*, 102, 14899-14913.
- Ruff, S. W., and Christensen, P. R. (2002). Bright and dark regions on Mars: Particle size and mineralogical characteristics based on Thermal Emission Spectrometer data. *Journal of Geophysical Research: Planets*, 107(E12), 2–1–2–22. doi:10.1029/2001je001580.
- Salisbury, J. W., Hapke, B., and Eastes, J. W. (1987). Usefulness of weak bands in midinfrared remote sensing of particulate planetary surface, *J. Geophys. Res.*, 92,702-710.
- Salisbury, J. W., and Eastes, J. W. (1985). The effect of particle size and porosity on spectral contrast in the mid-infrared. *Icarus*, 64(3), 586–588. doi:10.1016/0019-1035(85)90078-8.

- Salisbury, J. W. (1993). Mid-infrared spectroscopy: Laboratory data. In Remote geochemical analysis elemental and mineralogical composition. Cambridge, UK: Cambridge University Press. pp. 79–98.
- Salisbury, J.W., Walter, L.S., (1989). Thermal infrared (2.5-13.5 microns) spectroscopic remote sensing of igneous rock types on particulate planetary surfaces. *Journal of Geophysical Research*. 94, 9192–9202.
- Salisbury, J. W., D’Aria, D. M., and Jarosewich, E. (1991). Midinfrared (2.5–13.5 μm) reflectance spectra of powdered stony meteorites. *Icarus*, 92(2), 280–297. doi:10.1016/0019-1035(91)90052-u.
- Salisbury, J.W., Walter, L.S., Vergo, N. (1987). Mid-Infrared (2.1–25 μm) Spectra of Minerals, first ed. U.S. Geological Survey. Open-File Report 87-263, 365 pp.
- Salisbury, J. W., and Wald, A. (1992). The role of volume scattering in reducing spectral contrast of reststrahlen bands in spectra of powdered minerals. *Icarus*, 96(1), 121–128. doi:10.1016/0019-1035(92)90009-v.
- Shirley, K. A., McDougall, D., and Glotch, T. D. (2018). The Effect of Albedo on Mid-Infrared Spectra of Airless Bodies with Implications for Diviner Data Analysis. 49th Lunar and Planetary Science Conference, The Woodlands, TX.
- Shirley, K. A., and Glotch, T. D. (2019). Particle Size Effects on Mid-IR Spectra of Lunar Analog Minerals in a Simulated Lunar Environment. *Journal of Geophysical Research: Planets*. doi:10.1029/2018je005533.

- Stokes, G. G. (1850). On the Effect of the Internal Friction of Fluids on the Motion of Pendulums. Mathematical and Physical Papers, 1–10. doi:10.1017/cbo9780511702266.002.
- Thomas, I. R., Greenhagen, B. T., Bowles, N. E., Donaldson Hanna, K. L., Temple, J., and Calcutt, S. B. (2012). A new experimental setup for making thermal emission measurements in a simulated lunar environment. Review of Scientific Instruments, 83, 124502. doi:10.1063/1.4769084.
- Tyler, A. L., Kozlowski, R. W. H., and Lebosky, L. A. (1988). Determination of rock type on Mercury and the Moon through remote sensing in the thermal infrared. Geophysical Research Letter, 15, 808 – 811.
- Vincent, R. K., and G. R. Hunt 1968. Infrared reflectance from mat surfaces. Appl. Opt. 7, 53-59.
- Wang, X., Schwan, J., Hsu, H.-W., Grün, E., and Horányi, M. (2016). Dust charging and transport on airless planetary bodies. Geophysical Research Letters, 43(12), 6103–6110. doi:10.1002/2016gl069491.